

# Emissions and imaging studies of spark assisted HCCI

by

Peter Keros

A dissertation submitted in partial fulfillment  
of the requirements for the degree of  
Master of Science  
(Mechanical Engineering)  
in The University of Michigan  
2011

Defense Committee:

Professor Margaret Wooldridge, Chair  
Professor Zoran Filipi

© Peter Keros 2011

---

All Rights Reserved

to my brother, without whom I would not be the man I am  
today

# Acknowledgements

It would be an understatement to say that my success comes with the help of the dozens of people who have helped, influenced, guided, and served to bring me to this point.

I would like to thank my family for their unceasing support. You may not understand everything on these pages, but you have contributed to them nonetheless. Not to mention a spectacular catering job for my defense.

Special thanks go to my brothers of  $KK\Psi$ , particularly Sarah, RJ, Al, Paul, CWee, Eddie, Allie, Sierra, Marc, Joe, Tammi, and Malinda. You push me always to strive for the highest, and such an ambitious effort could not have been realized without all of your support. I certainly could not have balanced convention and my research without such excellent brothers.

I would also like to acknowledge my friends in the Michigan Marching Band and in  $TB\Sigma$ , notably my co-chairs for conven-

tion, Ellyn and Kristy. We laughed, we cried, and we pulled our hair out for two years to pull off an event unparalleled in my experience. I cannot express how much your hard work helped me to focus my time and energies.

Of course, where would I be without my engineering friends? I'd like to thank Carol, Jenn, Sarang, the Auto Lab folk, and all of the Steves for their support, whether it be on graduate council, lunch group, softball, or the Tea Party. Thank you for showing me the unique leadership that our department and its students have.

My labmates, Mohammad, Dimitri, both Steves, Darshan, Scott, Paul, Brad, Smitesh, and Jim, also deserve more gratitude than I can give. Without you all, I would probably have broken the engine beyond repair, set fire to the lab, and set up a coffee shop with the Henken burner. I will miss this office and the people within.

I would like to thank my committee members, Zoran Filipi, Aris Babajimopoulos, George Lavoie, and Jason Martz for their intriguing academic insight. You have challenged me to explore the world of engine research and look at combustion in a new light; for this, I am grateful.

Special thanks go to my advisor, Margaret Wooldridge. Funding

a Master's student is almost unheard of in today's PhD-driven world, and I appreciate the opportunity to work on such interesting research. Your encouragement and insight have helped me to become a better student, researcher, and leader. I look forward to using the many skills I have learned in this lab in law school and the legal field.

I know that there are people that I have forgotten to thank, so I give my gratitude to all of you here. Know that I will always appreciate your help and support.

*Soli deo gloria*

# Table of Contents

Dedication . . . . .	i
Acknowledgements . . . . .	ii
List of Figures . . . . .	viii
List of Tables . . . . .	xi
List of Appendices . . . . .	xii
Abstract . . . . .	xiii
Chapter	
1. Introduction . . . . .	1
2. Experimental Approach . . . . .	5
2.1 Optical Research Engine . . . . .	5
2.2 High Speed Imaging . . . . .	9

2.3	Instrumentation and Data Acquisition . . .	10
<b>3.</b>	<b>SA HCCI Emission Studies . . . . .</b>	<b>13</b>
3.1	Engine Conditions . . . . .	13
3.2	Effects of peak pressure . . . . .	15
3.3	Effects of heat release rate . . . . .	16
3.4	Effects of phasing of peak pressure . . . . .	18
3.5	Effects of spark timing . . . . .	20
<b>4.</b>	<b>Image Processing Methods . . . . .</b>	<b>23</b>
4.1	Raw Data Acquisition and Pre-Processing	23
4.2	Propagation Speed Measurement . . . . .	24
4.2.1	Image Thresholding . . . . .	25
4.2.2	Autoignition Image Processing Method . . . . .	25
4.2.3	Edge Front Calculation . . . . .	28
4.3	Initial Investigation . . . . .	30
4.3.1	Flame Speed Comparison . . . . .	30
4.3.2	Multicycle Analysis . . . . .	32
4.3.3	Uncertainty Analysis: Image Pro- cessing Parameter Effects . . . . .	33
<b>5.</b>	<b>Imaging Results . . . . .</b>	<b>37</b>
5.1	Apparatus Settings for Imaging Study . . .	37
5.1.1	SCORE Settings . . . . .	38
5.1.2	Camera Settings . . . . .	38
5.1.3	Image Processing . . . . .	39
5.2	Experimental Results . . . . .	39



---

5.2.1	Experimental Settings . . . . .	39
5.2.2	Equivalence Ratio Effects . . . . .	42
5.2.3	Spark Timing Effects . . . . .	49
5.3	Estimates for In-Cylinder Temperature . . . . .	56
5.3.1	Temperature Estimation Algorithm . . . . .	57
5.3.2	Midrange Condition Temperatures . . . . .	57
5.3.3	Lean Condition Temperatures . . . . .	58
5.3.4	Estimated Autoignition Temperature Comparison . . . . .	61
5.4	Comparison to Detailed Image Analysis . . . . .	63
5.4.1	Manual Image Analysis . . . . .	63
5.4.2	Spatial Resolution of Edge Front Method . . . . .	66
<b>6.</b>	<b>Conclusions and Future Work . . . . .</b>	<b>69</b>
6.1	Conclusions . . . . .	69
6.2	Future Work . . . . .	71
<b>Appendices</b>	<b>. . . . .</b>	<b>73</b>
A.1	Experimental Data Tables . . . . .	74
A.2	Emissions Experiments Engine Data . . . . .	80
A.3	Imaging Experiments Engine Data . . . . .	89

# List of Figures

## Figure

3.1	Emissions plotted against peak pressure . . . . .	15
3.2	Emissions plotted against peak HRR . . . . .	17
3.3	Emissions and HRR plotted against phasing of maximum pressure. 0 indicates TDC; positive values are after TDC, negative values, before. . .	19
3.4	Phasing at each spark timing. 0 on SA axis indicates HCCI; positive values are before TDC. 0 on phasing axis indicates TDC; positive values are after TDC. . . . .	21
4.1	Image with 1% threshold applied. The green circle is the limit of the viewing area. . . . .	26
4.2	Image converted to equivalent area. . . . .	27
4.3	Results of edge traced around thresholded image.	28

---

4.4	Equivalent circles determined from orthogonal dimension lengths. . . . .	29
4.5	Comparison of $V_I$ and $V_{II}$ for one cycle of SA HCCI operation. $T_{in} = 350^\circ\text{C}$ , $\phi = 0.54$ . . . . .	31
4.6	Flame speed data from five cycles. . . . .	32
4.7	Images with different parameter processing. The top row consists of the unaltered images; the middle row, the clarified images; the bottom row, the 5% threshold images. . . . .	35
4.8	Flame speed data for modified images. . . . .	36
5.1	$V_I$ and HRR data for unassisted HCCI experiments . . . . .	42
5.2	$V_{II}$ and HRR data for $20^\circ$ BTDC spark assist experiments . . . . .	45
5.3	$V_{II}$ and HRR data for $40^\circ$ BTDC spark assist experiments. Bottom image included to clarify flame propagation. . . . .	47
5.4	Flame propagation rate and HRR data for experiments R0, R20, and R40. . . . .	50
5.5	Sequential images from a representative cycle from experiment R20. . . . .	51

5.6	Flame propagation rate and HRR data for midrange equivalence ratio conditions. . . . .	52
5.7	Flame propagation rate and HRR data for lean equivalence ratio conditions. . . . .	55
5.8	Temperature profile for midrange conditions. . .	59
5.9	Temperature profile for lean conditions. . . . .	60
5.10	Temperature and velocity profiles for selected midrange conditions . . . . .	62
5.11	Average cardinal velocity diagram. . . . .	64
5.12	Framewise cardinal flame front diagram. $T_{in} = 271^{\circ}\text{C}$ , $\phi = 0.45$ , SA20. . . . .	65
5.13	Cardinal and average velocity measurements. . .	66
5.14	Average velocities for all cycles. . . . .	67
5.15	Directional dimensions compared to $V_{II}$ for L40.	68

---

# List of Tables

## Table

4.1	Image Processing Parameter Settings for Clarified Images . . . . .	34
5.1	Experimental conditions for imaging study. Experiments are listed by equivalence ratio, ranging from rich to lean. . . . .	40
5.2	Engine and emissions data averaged over 27 cycles	41
5.3	Engine and emissions data averaged over 27 cycles.	50
5.4	Estimated autoignition temperatures of midrange and lean engine conditions. . . . .	61
A.1	Experimental Data - Emissions . . . . .	74
A.2	Experimental Data - Engine Metrics . . . . .	76
A.3	Experimental Data - Engine Metrics . . . . .	78
A.4	Experimental data from emissions experiments.	80
A.5	Experimental data from imaging experiments. .	89

# List of Appendices

## Appendix

A. Engine Experimental Data . . . . . 74

# Abstract

Homogeneous charge compression ignition (HCCI) has the potential to improve engine efficiency while reducing tailpipe emissions; however, controlling HCCI over the broad range of speed and load conditions common to internal combustion (IC) engines remains a challenge. Spark assist (SA) has potential to improve HCCI operation, but the mechanisms that enable and conversely limit SA are not well known. The objective of this work was to identify the physical and chemical mechanisms important during SA HCCI engine operation. A series of experiments were conducted to study the engine performance characteristics, including engine power, efficiency and emissions of HCCI and SA HCCI. In-cylinder, high speed imaging data were also acquired. A wide range of intake temperatures (260–360°C), equivalence ratios ( $\phi = 0.4\text{--}0.6$ ), and spark timings (10–70° BTDC) were selected to investigate stable and unstable HCCI and SA HCCI conditions.

Two novel and fast methods for analyzing the chemiluminescent images were developed for the in-cylinder optical data. A brightness threshold was applied to the color images, converting the images to black and white stills. In one method, designed to quantify the properties of the autoignition events, an equivalent circular area was calculated from the image, the radius of

which was used to calculate the speed of the autoignition process,  $V_I$ . In the second method, an edge finding function was applied to the thresholded image. The maximum dimensions in the 2-dimensional orthogonal Cartesian coordinate system were then measured and averaged to create an equivalent circle circumscribing the image. The average diameter was then used to calculate the rate of propagation of the expanding flame front,  $V_{II}$ . The results of the new image analysis methods are in good agreement with other image analysis methods that are more spatially accurate, but considerably more time consuming.

The methods were used to analyze the series of HCCI and SA HCCI experiments and the results were compared with the engine data. SA had a clear impact on ignition phasing within a window of operating conditions. Specifically, if in-cylinder conditions resulted in fast and early autoignition (typically high preheat and/or high equivalence ratios, where ignition occurred 5–10 crank angle degrees before top dead center), SA had limited impact on ignition phasing and consequently efficiency and emissions. If in-cylinder conditions resulted in late autoignition or misfire (typically low preheat and/or low equivalence ratio conditions), SA advanced ignition compared to unassisted HCCI. The imaging data show flames were successfully initiated at all conditions by SA, and the flames were not associated with increased heat release rates compared to HCCI. Flame-like characteristics were never observed in the absence of SA. Comparison of stable HCCI and SA HCCI conditions indicate the flames produced by SA are not significant sources of  $\text{NO}_x$  emissions.

The combination of the imaging and the engine performance data provide new insights to effectively use SA to improve HCCI



operation. For example, the results have implications on how to apply SA at high load conditions to distribute the pressure rise and heat release rate. The imaging data demonstrate that flames are consistently initiated by SA, and exhibit speeds that typically accelerate from 1 m/s to 4 m/s. If HCCI produces autoignition events that propagate faster than this rate, SA has limited effect, even though flames are initiated by the spark.



# Chapter 1

## Introduction

Modern energy concerns pose difficult challenges for engineers; challenges requiring robust and dynamic solutions that include the fundamental nature of energy transfer processes. The ubiquity of hydrocarbon combustion is an obvious direction that energy scientists can take; improvements in combustion can create significant reduction in environmental impact. The trend toward lean, low temperature combustion (LTC) stems from a desire to lower pollutant emissions, most notably nitric oxides ( $\text{NO}_x$ ) and particulate emissions (PM). While improving engine efficiency, the challenge with LTC lies in both the fundamental combustion characteristics and the implementation in modern technology.

The advent of homogeneous charge compression ignition (HCCI) as a new automotive combustion strategy provides a potential

solution with many of the advantages of LTC which is achievable in current and near-future engines. HCCI engines have several potential advantages over traditional spark ignition (SI) engines, most notably they offer greater fuel economy while simultaneously lowering  $\text{NO}_x$  and soot emissions [1, 2]. The increase in fuel economy comes from the ability of HCCI engines to operate with higher compression ratios and reduced throttling losses, while the reduction of nitric oxides comes from the lower in-cylinder temperatures compared to SI or diesel engines. The homogeneity of the mixture eliminates local rich zones, and since the global equivalence ratio of HCCI operation tends to be very lean ( $\phi < 0.6$ ), particulate emissions are nearly zero. In a sense, HCCI provides a combination of the advantages of SI operation, the gasoline infrastructure with low PM emissions, with the advantages of diesel operation, high compression ratio and globally lean mixtures.

HCCI engines have some unique challenges, primarily stemming from the dependence on chemical kinetics for combustion rather than a traditional control strategy such as spark ignition or injection timing. The load range over which HCCI operation is viable is small compared to the urban driving cycle. At the low load limit, the charge does not have enough energy to initiate ignition, so misfire occurs, while at the high load limit, ignition is so strong and fast that knock occurs, potentially damaging

---

the engine. A number of strategies have been proposed to extend these limits and improve the viability of HCCI, including spark assist [3, 4, 5, 6, 7, 8, 9, 10], variable valve timing [3, 11] and variable compression ratio [5, 12, 13] methods.

Many of these methods show promise, particularly spark assisted HCCI (SA HCCI). Spark assist has been demonstrated to improve transition between SI and HCCI modes of operation [3, 5, 14] and to expand the mode of acceptable HCCI operation [8]. Initial optical studies have been performed, both with chemiluminescent optical imaging and PLIF [4, 15, 16, 17]. The studies by Johansson in particular showed estimates for the flame speed derived from the optical images using flame area differencing normalized by the flame perimeter [16].

The University of Michigan has contributed to this field as well, primarily through the use of the single-cylinder optical research engine (SCORE) initially constructed by Dr. Brad Zigler [10, 18, 19, 20, 21]. An imaging study examining three fuels (iso-octane, pump gasoline, and indolene) was conducted by Dr. Zigler to determine the fuel combustion characteristics in the UM SCORE [19]. A multiaxis imaging study of SA HCCI was conducted showing both planar and axial views of the combustion events [21]. Dr. Zigler's work ultimately culminated in a thorough investigation of SA HCCI, including the potential to extend the

lower limit of HCCI operation. During this work, two distinct regimes of combustion were identified: flame propagation and autoignition [10].

The objective of this study was to identify the physical and chemical mechanisms important during SA HCCI engine operation. While a number of studies on HCCI emissions have been conducted, very few have investigated SA HCCI and the potential impact on  $\text{NO}_x$  and unburned hydrocarbons (HC). This study examines emissions, imaging, and engine performance over a range of engine operating conditions in both HCCI and SA HCCI in order to identify links between in-cylinder ignition events and engine performance. Chemiluminescent imaging of HCCI and SA HCCI has been examined before, but this study presents new and fast image processing methods that quantify flame speeds and can be applied to large volumes of data, giving insight into the fundamental nature of HCCI and SA HCCI combustion.

# Chapter 2

## Experimental Approach

The SCORE (single-cylinder optical research engine) at the University of Michigan has changed little, but crucially, since the initial construction by Dr. Brad Zigler. The primary objective of the SCORE is to provide improved understanding of the chemical and physical mechanisms important in advanced engine systems, including HCCI, spark-assisted HCCI, and other low temperature combustion strategies.

### 2.1 Optical Research Engine

All experiments were conducted using the UM SCORE. This facility is based on an optical research engine donated by the Ford Motor Company and designed conceptually based on the

optical research engine developed by Sandia National Laboratory [22]. The SCORE features a hydraulically-supported, drop-down cylinder liner assembly with interchangeable fused silica and steel cylinder liners supporting a Bowditch-style piston extension with a quick-release top piston. The piston features a removable crown insert window, made of either fused silica or aluminum. An elliptical mirror is fixed in the piston extension for optical access through the  $\varnothing 48.5$  mm piston window. The resulting facility offers excellent axial and orthogonal optical access through the piston window/mirror and the cylinder liner, respectively.

The SCORE is built around a Ford Zetec-SE 1.25 L engine configuration, originally built in Valencia, Spain for the 1997 Ford Fiesta (European). A modified production cylinder head is used, employing one of the four cylinders available. The aluminum cylinder head features fixed double-overhead cams timing four valves (twin  $\varnothing 26.1$  mm intake, twin  $\varnothing 22.1$  mm exhaust) around a centrally mounted spark plug. A flat-top  $\varnothing 71.9$  mm piston with Torlon rings strokes 76.5 mm for 0.31 L displacement at 10:1 compression ratio. Fuel is port injected slightly upstream of the twin intake ports.

The engine is driven by a Micro-Dyn 35 hydraulic dynamometer. Typical experiments hold the engine speed constant at  $700 \pm 5$



RPM. The hydraulic dynamometer has an automatic control system to maintain set speed by compensating between providing a motoring load and absorbing net power output. Engine coolant and oil are auxiliary heated; coolant was maintained at 90 °C and oil was maintained at 60 °C. The engine was typically pre-conditioned by circulating heated coolant for at least 45 minutes. The engine was then motored by the dynamometer for another 30 minutes to stabilize oil temperature and intake air conditions before running experiments.

Fuel was fed to the Siemens DEKA II center-feed dual conical jet injector at a fixed fuel pressure of 1.7 atm. An Electro-Mechanical Associates Engine Control Module (ECM) spark and fuel injection controller is integrated with the dynamometer. Fuel equivalence ratio was controlled by varying the fuel injector driver pulse width duration, holding fuel rail pressure constant. Equivalence ratio was measured using a lambda sensor located in the exhaust, which is described below.

All experiments in this study were run unthrottled or Wide Open Throttle (WOT), with the fuel injection pulse width varied to control the overall equivalence ratio of the fuel/air mixture. While this caused various equivalence ratios to have different engine loadings, the fixed open throttle plate setting and subsequent removal of the throttle assembly allowed fewer changes

to the engine operating conditions to achieve HCCI for various equivalence ratios.

Fuel was injected very early onto a closed intake valve, at either  $50^\circ$  before top dead center (BTDC) or at top dead center (TDC) during the compression stroke of the preceding cycle, to assist fuel vaporization and mixing with the intake air. The intake air was heated using three different apparatus over the course of this study. Initially, the ambient air was preheated with a 1.4 kW heater and the intake manifold was heated using an auxiliary resistive heater to deliver various intake air temperatures of approximately  $250\text{--}360^\circ\text{C}$  just upstream of the fuel injector. Note, the thermocouple measurement at this location is not the cylinder charge temperature. This is the setup for the first set of experiments which helped to characterize emission levels, described in Chapter 3. The heater was replaced with a Furman 2 kW flow torch controlled electronically by a LabView PID controller program. This system was used for the initial imaging method development, described in Chapter 4. A storage tank was added with fin heaters to dampen air flow acoustics and preheat air to about  $250^\circ\text{C}$ . The air then flows through the flow torch to further increase the temperature to  $280\text{--}380^\circ\text{C}$ . Both heaters are controlled with a LabView PID controller program.

## 2.2 High Speed Imaging

The combustion chamber was imaged through the piston window using a high-speed color digital video camera (Vision Research Phantom v7.1, color). The camera is capable of 800 x 600 pixel spatial resolution, and reduced resolution frame rates up to 160 kHz. A fast 50 mm lens (f/0.95 Nikor TV lens) and C-mount extension tubes are used with the camera to adjust the focal length and to reduce the focal depth along the cylinder axis. In this study, the camera was focused at a plane coinciding with the spark plug ground electrode. The camera settings were generally fixed at 320 x 320 pixels for piston window imaging (or 640 pixels wide x 480 pixels high for orthogonal imaging through the transparent cylinder liner) at 3000 frames per second (fps) with 309  $\mu$ s exposure time or 5000 fps with 100  $\mu$ s exposure time. The camera sensor array was calibrated according to the procedure outlined in Walton et al. [23] The piston window is  $\varnothing$ 48.5mm, which partially occludes the valves. Recall the piston diameter is  $\varnothing$ 71.9 mm. Thus, 45.5% of the projected area of the cylinder is imaged.

Non-filtered, visible chemiluminescence emission was recorded via the high-speed color digital camera and time-sequenced with crank-angle resolved pressure data. Camera images were time sequenced to a common trigger with other data, and were color

and gain adjusted to improve image viewing clarity. All time-recorded data were then transcribed into a crank-angle basis with respect to compression stroke TDC.

## 2.3 Instrumentation and Data Acquisition

Cylinder pressure is measured using a piezoelectric transducer (Kistler 6125A) and charge amplifier (Kistler 5010B). Intake pressure is measured with an absolute pressure sensor in a water cooled fitting (Kistler 4045A2 with Kistler 4618 amplifier). The water cooled fitting is necessary for the intake pressure sensor to protect it against high intake temperatures. Pressure data were not filtered prior to recording.

Crank angle is encoded with a BEI encoder at 360 signal cycles per revolution, with a secondary channel output signaling TDC. In addition to the aforementioned intake manifold thermocouple, other thermocouples record coolant temperature leaving the cylinder head, and oil temperature entering the engine.

Equivalence ratio is measured in the exhaust manifold using an ETAS LA4 lambda meter utilizing a Bosch broadband LSU 4.9 lambda sensor. The lambda meter calculates equivalence ratio based on the  $O_2$  content of the exhaust stream, given the fol-

lowing inputs:

- fuel H/C ratio
- fuel O/C ratio
- fuel H<sub>2</sub>O component
- stoichiometric air / fuel mass ratio

Since the lambda meter falsely reads excess exhaust O<sub>2</sub> due to incomplete combustion and misfire as a mixture leaner than actual, some procedural development was required. For each intake temperature, a series of experiments were conducted to map the relationship between fuel pulse width and the ETAS LA4 lambda meter measurements. For lean mixtures which resulted in incomplete combustion in HCCI mode, advanced spark ignition was used to provide more complete combustion in the same pulse width. The equivalence ratio for that more complete combustion condition was then used as a reference for that particular fuel pulse width / intake temperature combination. This procedure helped correct readings for most lean mixtures which experienced high misfire. Corrections for very lean conditions were also estimated by interpolation from other conditions.

Data acquisition for the pressure data and CAD encoder was performed using a National Instruments Compact Data Acqui-

sition (cDAQ). This universal serial bus based system recorded temperature readings at the beginning of each experiment, then recorded all digital and analog channels at 100 kHz, using a LabView software code.

Emissions were measured using a Horiba MEXA-584L exhaust gas analyzer. The exhaust gases were sampled approximately 3 cm from the exit of the exhaust valves. Unheated metal tubing approximately 110 cm in length was used to transport the exhaust gases through a water filter, after which approximately 30 cm of plastic tubing transported the gases to the analyzer.  $\text{NO}_x$ , CO and HC emissions were measured using this device.

# Chapter 3

## SA HCCI Emission Studies

In order to understand the emissions characteristics of the UM SCORE's operation and HCCI combustion in general, a comprehensive range of engine conditions were examined, and a data set consisting of engine metrics (such as pressure and heat release rate) and emissions data ( $\text{NO}_x$  and HC) was compiled. No imaging data were taken for these studies; the metal piston insert was used instead of the quartz.

### 3.1 Engine Conditions

A wide range of intake temperatures, equivalence ratios, and spark timings were examined to investigate engine performance

and emission formation. The complete set of conditions is listed Table A.

Intake temperatures ranged from 260–360°C, allowing for a wide range of combustion modes, including marginal HCCI conditions where spark assist prevented misfire and strong HCCI conditions where spark assist had little effect on the robust autoignition. Equivalence ratios ranged from  $\phi = 0.4$ –0.6, and spark timings ranged from 10–50° BTDC.



### 3.2 Effects of peak pressure

Since temperature drives the majority of  $\text{NO}_x$  production in IC engines, and since in-cylinder pressure indicates temperature,  $\text{NO}_x$  values and peak cylinder pressure should relate directly. As Figure 3.1 shows, increasing peak pressure will generally lead to higher  $\text{NO}_x$  values. The trend, however, is not monotonic;  $\text{NO}_x$  values are fairly constant at low pressures until 28 bar, after which the  $\text{NO}_x$  rises exponentially with the pressure. As  $\text{NO}_x$  increases, HC decreases, though its magnitude is much smaller; this implies a  $\text{NO}_x$ -HC tradeoff.

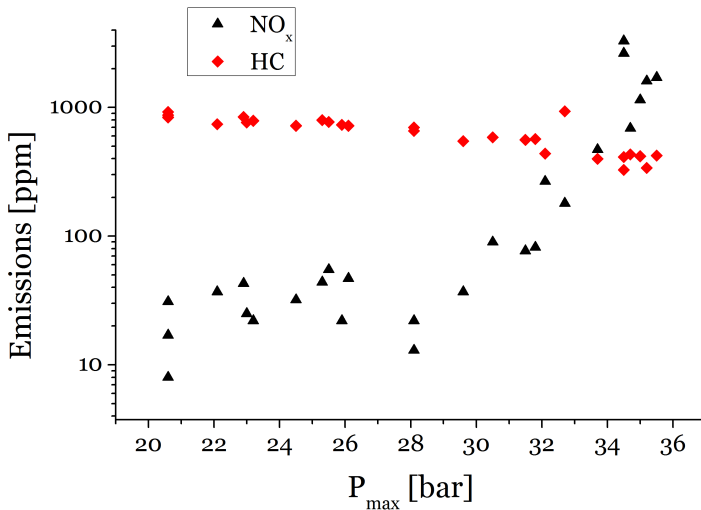


Figure 3.1: Emissions plotted against peak pressure

### 3.3 Effects of heat release rate

While peak cylinder pressure can be a good trend indicator of global temperature, investigating heat release rate might provide better insight into the thermal characteristics of the combustion. Higher rates of heat release could induce higher temperatures, and thus higher  $\text{NO}_x$ . HRR was determined using the classic thermodynamic relation from Heywood's textbook,

$$\frac{dQ}{dt} = \frac{\gamma}{\gamma - 1} p \frac{dV}{dt} + \frac{1}{\gamma - 1} V \frac{dp}{dt} \quad (3.1)$$

where  $p$  is the in-cylinder pressure, as measured by our transducer,  $V$  is the instantaneous volume, determined using the geometry and speed of the engine, and  $\gamma$ , the ratio of specific heats, was estimated to be 1.35 based on similar estimation by Zigler. [24, 10] Figure 3.2 shows the emissions plotted against peak HRR. The trend here is clearer: increasing HRR leads to higher  $\text{NO}_x$  (and lower HC) values. There is a bit of scatter, such as a point around 30 J/CAD whose  $\text{NO}_x$  values are significantly higher than those for a few experiments with higher HRR. Overall, HRR can be a good indicator of  $\text{NO}_x$ , but further investigation into other metrics could prove useful.

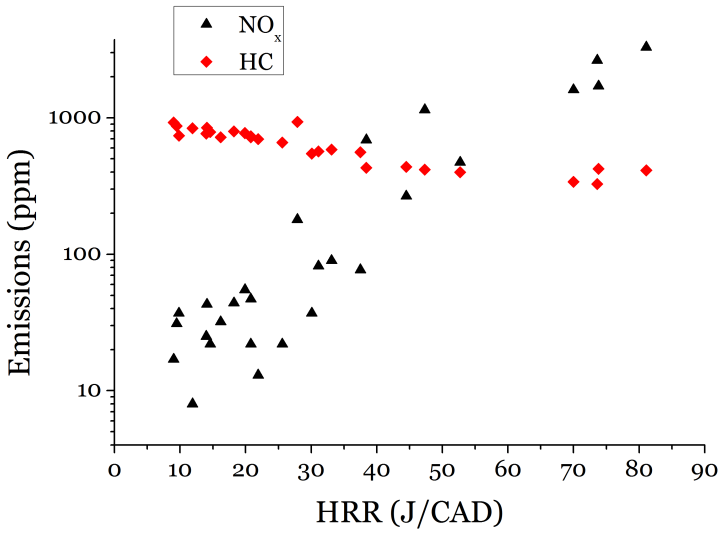


Figure 3.2: Emissions plotted against peak HRR

### 3.4 Effects of phasing of peak pressure

While peak pressure and HRR both show good emissions trends, one metric of interest is the phasing of peak pressure. The phasing can give insight into how quickly the combustion is occurring, and thus insight into the temperature changes that might affect emissions. Figure 3.3 shows the emissions and HRR as a function of phasing of peak pressure.

The trend is striking. For both HCCI and SA HCCI and regardless of intake temperature, if the phasing is before TDC, the likelihood of  $\text{NO}_x$  values above 1000 ppm is very high, while *all* experiments after TDC are below 1000 ppm, and after  $2^\circ$  ATDC, all are below 100 ppm. Consequently, due to the  $\text{NO}_x$ -HC tradeoff, HC emissions are low if the phasing is before TDC, while they rise if the phasing is later.

The trend in HRR is remarkably similar to the  $\text{NO}_x$  trend, with higher HRR before TDC and lower HRR after. Note that the emissions are plotted on a log scale, while the HRR is plotted on a linear scale; the similarity in the trends is reminiscent of Figure 3.2, showing a reasonably clear trend between HRR and  $\text{NO}_x$ .

Of all the various engine metrics, the trend here is most evident.

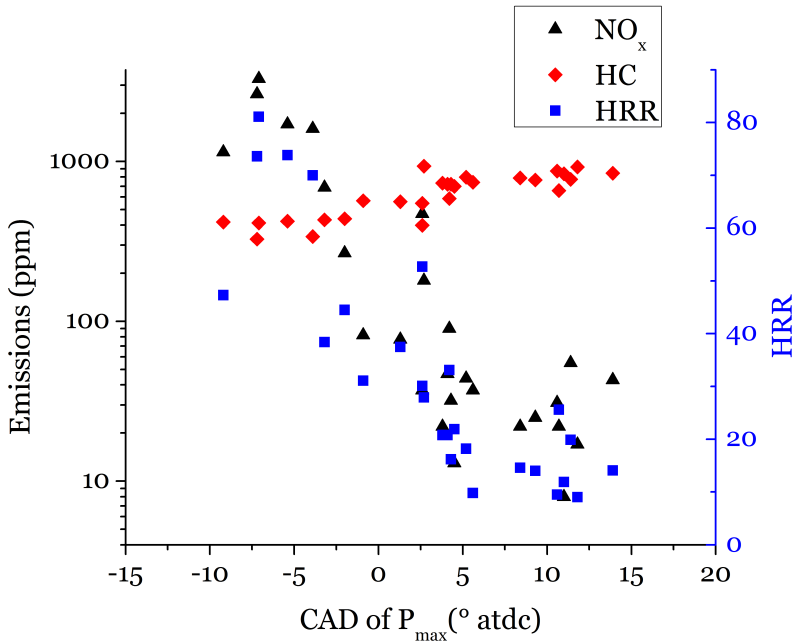


Figure 3.3: Emissions and HRR plotted against phasing of maximum pressure. 0 indicates TDC; positive values are after TDC, negative values, before.

Early phasing is a clear sign that  $\text{NO}_x$  levels will be high, implying that the in-cylinder temperatures for these experiments is much higher than experiments with later phasing. It is this crucial parameter that further studies will attempt to control.

### 3.5 Effects of spark timing

Being the primary focus of SA HCCI, the effects of spark timing on emissions were investigated. Of particular interest is whether the spark plasma increases  $\text{NO}_x$  emissions by causing local hot regions. Since spark timing would likely affect phasing most directly, and based on the strong relation between phasing and emissions, phasing was measured against spark timing, as seen in Figure 3.4.

At each spark timing, phasing values range both before and after TDC. Of note is that for the  $20^\circ$  BTDC and  $30^\circ$  BTDC spark assist experiments, there are very few that have phasing before TDC, while the other spark timings and the unassisted condition had more distribution around TDC. The spark timing as a whole does not seem to have a consistent effect on HCCI combustion. Of note is that the spark plasma does not seem to increase  $\text{NO}_x$  emissions significantly, especially when compared to phasing.

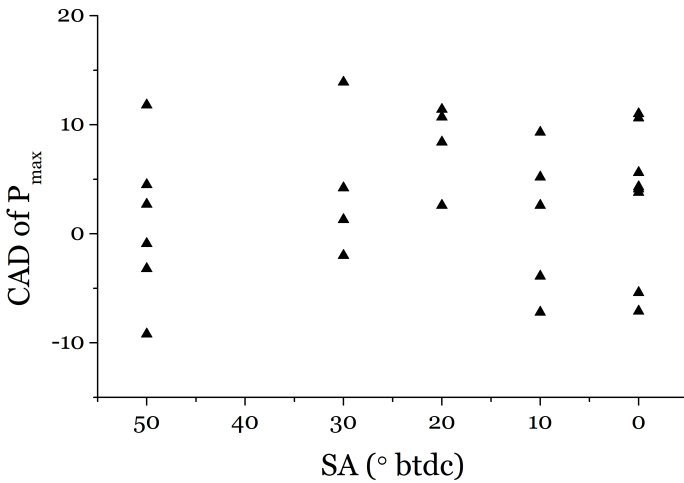


Figure 3.4: Phasing at each spark timing. 0 on SA axis indicates HCCI; positive values are before TDC. 0 on phasing axis indicates TDC; positive values are after TDC.

Overall, the data presented show that the best indicator for high  $\text{NO}_x$  emissions is phasing of maximum pressure before TDC. No other metric examined here had such a clear impact on emissions, with a few degrees difference altering emissions by multiple orders of magnitude. The key to utilizing HCCI and SA HCCI while maintaining low emissions lies in the ability to control phasing.



# Chapter 4

## Image Processing Methods

Upon acquiring chemiluminescent imaging data, the images must be processed to extract quantitative information. The methods by which the images are processed are explained in this chapter.

### 4.1 Raw Data Acquisition and Pre-Processing

The Phantom camera natively takes imaging data and stores it as a .cine movie file, a proprietary file type that can be used with the Phantom Vision software. This file can then be converted into a number of different types, from an .avi movie to .jpg or .tiff still images.

The Phantom Vision software can be used to clarify the images, modify RGB values and  $\gamma$  effects, and change contrast

and brightness settings. For the purposes of this study, the .cine movies were converted into a series of 8-bit .jpg stills before further processing. These files were then used as the basis for the image measurements.

## 4.2 Propagation Speed Measurement

Previous work identified two distinct regimes of combustion in HCCI and SA HCCI operation: autoignition and flame propagation [10]. For the autoignition regime, ignition occurred rapidly in parcels of fuel/air mixture resulting in volumetric autoignition of the parcels; this is referred to as “Regime I” [10]. The flame propagation regime is characterized by a reaction front forming and propagating throughout the combustion chamber; this is referred to as “Regime II.” The purpose of the image processing is to determine reaction propagation rates for the two regimes. Since they have distinct characteristics, different processing methods were developed. The methods were designed to be robust and able to process large volumes of imaging data in a short amount of time. The image sequences typically showed autoignition zones (Regime I) during HCCI operation, reaction front propagation (Regime II) during SA HCCI operation, and occasionally SA HCCI exhibited both types. The following sec-

tions describe in detail the methods by which propagation speed was measured.

### 4.2.1 Image Thresholding

The first step in both image processing methods is the thresholding of the color images into monochrome. The color files exist as three hexadecimal matrices, one for each of the red, green, and blue (RGB) values. Each pixel has a value indicating the brightness of the three colors. By applying a threshold, pixels with brightness above a certain value (a threshold) are defined as a single white pixel, while pixels below this threshold are defined as a black pixel. Thus, the image is converted from a set of RGB matrices into a single binary matrix consisting of black and white pixels. Figure 4.1 shows an example of an image before and after applying a 1% threshold. The brighter blue areas in the original image are converted into white pixels, while the darker areas remain black. At this point, the images can be analyzed by one of two methods depending on whether the combustion was dominated by autoignition or front propagation.

### 4.2.2 Autoignition Image Processing Method

The method presented here is used to find the propagation speed of an autoignition event, referred to as Regime I. Starting with

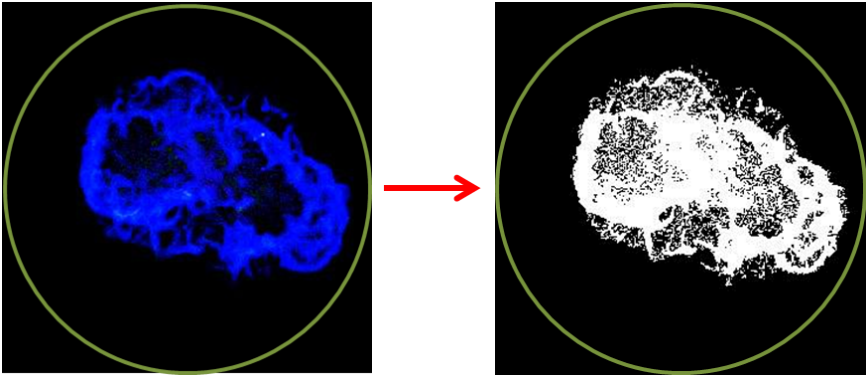


Figure 4.1: Image with 1% threshold applied. The green circle is the limit of the viewing area.

the thresholded image, an equivalent disc is formed with the same number of pixels as the original image. Figure 4.2 shows an example of such an image. The fractional area of the image where reaction occurred was then defined as

$$f = \frac{\sum \text{white pixels}}{\text{total pixels}} \quad (4.1)$$

where the *total pixels* correspond to an area  $A_0$  of 1876 mm<sup>2</sup> or the viewable area of the chamber. From here, the radius of the equivalent disc was determined with the following equation:

$$r_I = \sqrt{\frac{A_0 f}{\pi}} \quad (4.2)$$

Using the radius of this disc, the characteristic speed  $V_I$  was determined using the known timestep  $dt$  between frames and the change in radius  $dr_I$ :

$$V_I = \frac{dr_I}{dt} \quad (4.3)$$

The speed has the subscript  $I$  since it is useful for determining speeds for Regime I ignition. Consequently, the  $V_I$  data are used when analyzing HCCI conditions.

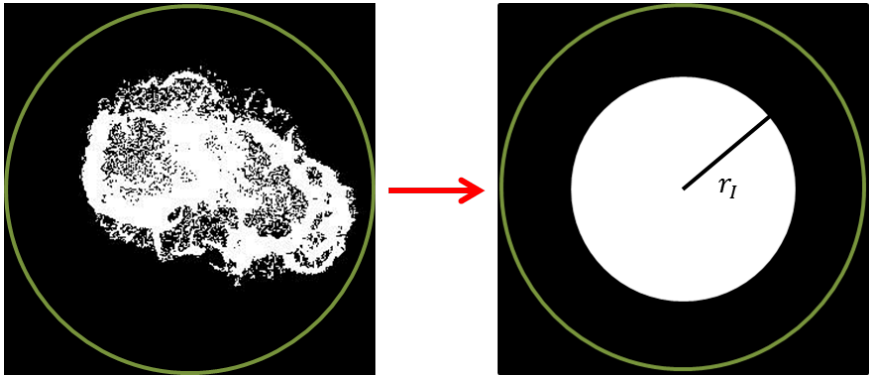


Figure 4.2: Image converted to equivalent area.

### 4.2.3 Edge Front Calculation

For conditions where reaction fronts were observed, a different imaging approach was developed to track changes in spatial dimensions that are ignored in the area calculation. Starting with the thresholded image, an edge-finding function was applied to create a 1-pixel width trace around the edge of the image. The number of pixels along the orthogonal axes  $x$  and  $y$  are measured in the image, giving maximum pixel dimensions in the  $x$  and  $y$  coordinates. The maximum dimensions are used to represent diameters of equivalent circles that act as upper and lower bounds of the outer edge of the flame front. This method allows spatial variations in the orthogonal directions to be accounted for in the flame speed calculation. [25]

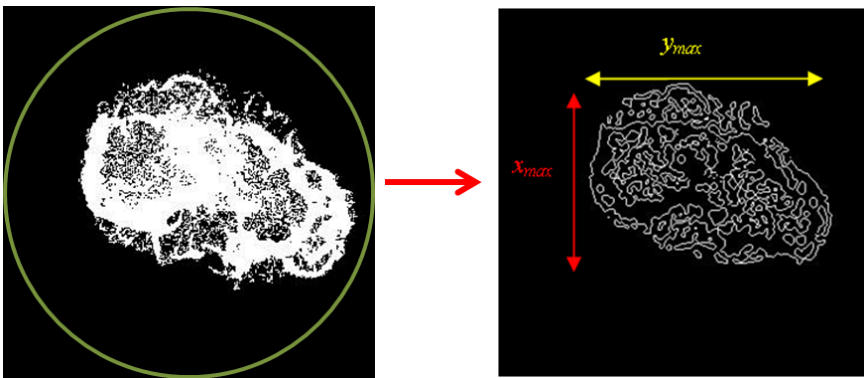


Figure 4.3: Results of edge traced around thresholded image.

The average of the two diameters is used to represent the area of the flame front as an equivalent circle. The radius of the circle is taken as  $r_{II}$ , and the change of  $r_{II}$  over time is  $V_{II}$ , so named since it is useful for measuring flame propagation, or Regime II, data.  $V_{II}$  data are used when analyzing SA HCCI conditions.

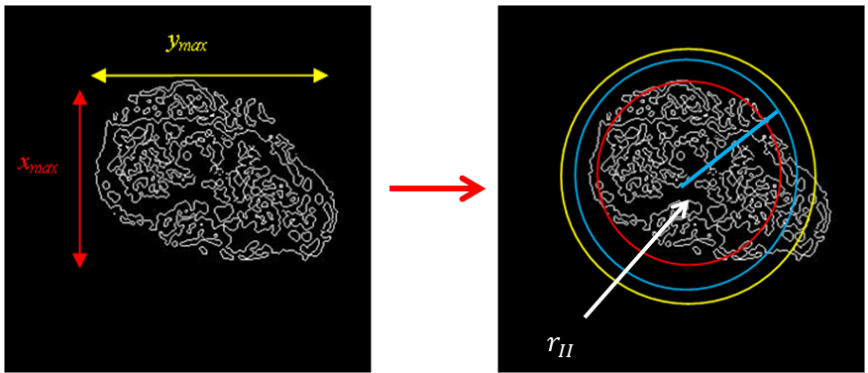


Figure 4.4: Equivalent circles determined from orthogonal dimension lengths.

$$d_{eq} = \frac{1}{2} (x_{max} + y_{max}) = 2r_{II} \quad (4.4)$$

$$V_{II} = \frac{dr_{II}}{dt} \quad (4.5)$$

## 4.3 Initial Investigation

In order to test the image processing methods, five cycles of SA HCCI operation were examined and processed. For these experiments, intake temperature was fixed at 350°C,  $\phi = 0.54$ , spark assist was fixed at 30° BTDC. Images were taken at 5000 fps with an exposure time of 100  $\mu\text{s}$ .

### 4.3.1 Flame Speed Comparison

Looking at the two flame speed calculations in one cycle offers some insight into the effects of the different image processing when applied to the same images.

The two methods yield comparable average speeds that show a steady increase in the flame speed until the major volumetric ignition event occurs.  $V_{II}$  yields more data variance, resulting in a negative propagation speed early in the imaging time history. The negative speed is an artifact of the image processing; it indicates the spark kernel extinguishing or shrinking prior to the formation of a self-sustaining and expanding reaction front. The  $V_I$  data do not exhibit this characteristic of the imaging sequence for this operating condition. Both flame speed calculations slowly accelerate from 0-5 m/s before autoignition. Ultimately, the trends are similar for both flame speed calculations



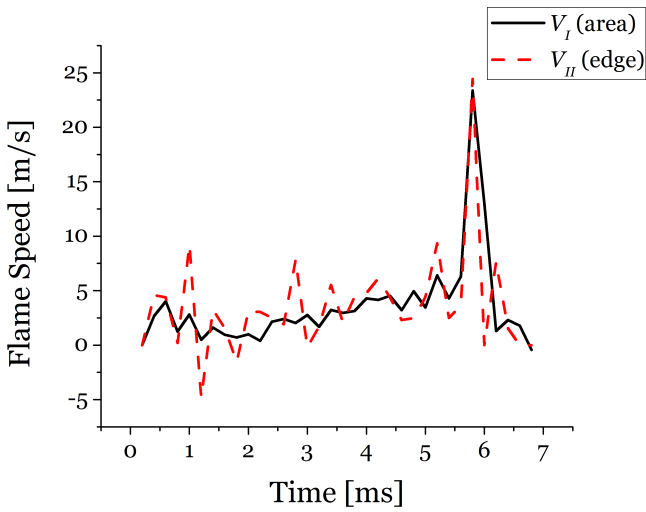


Figure 4.5: Comparison of  $V_I$  and  $V_{II}$  for one cycle of SA HCCI operation.  $T_{in} = 350^\circ\text{C}$ ,  $\phi = 0.54$ .

despite the difference in approach.

### 4.3.2 Multicycle Analysis

Cycle-to-cycle analysis is necessary to examine the variability in the imaging data. In the UM SCORE setup, imaging data are often taken for 30–50 cycles, so cycle-to-cycle data are readily available. For this study, five cycles of imaging data were analyzed, and the flame speeds are superimposed in Figure 4.6. The data are synchronized such that their peaks, indicative of autoignition, are aligned.

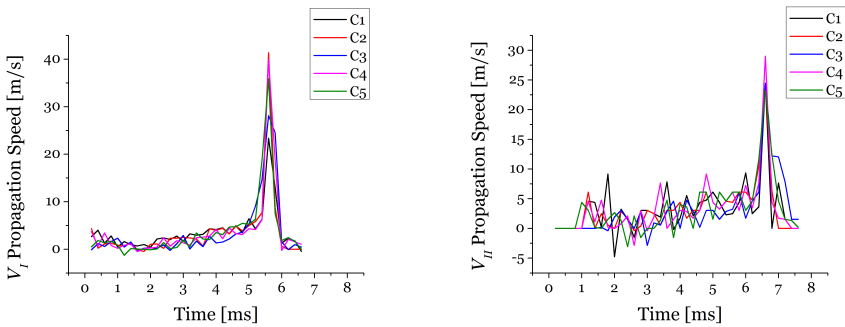


Figure 4.6: Flame speed data from five cycles.

The flame speed data are remarkably consistent. Flame speeds rise from 0–5 m/s for both  $V_I$  and  $V_{II}$  data before autoignition. The  $V_{II}$  data have a little more variance, but across cycles, the trends are consistent.

### 4.3.3 Uncertainty Analysis: Image Processing Parameter Effects

Throughout this discussion, the image processing has been the same for all of the data presented. The color images were unaltered, and a 1% threshold was applied to all images. At these settings, the initial images are moderately visible to the naked eye, and most of the shape is preserved upon thresholding. The Phantom software allows for altering of the images, so an investigation into the effects of various alterations and their effect on the uncertainty of the flame speeds was performed. One cycle of imaging data was taken and modified in two distinct processes. The first process clarified the image so that the initial color images are more visible to the naked eye; these are hereto referred as the “clarified” images. The second process applied a 5% brightness threshold to the unaltered images, essentially limiting the number of pixels in the final thresholded image and examining the effect of the threshold on the flame speed calculation. The parameter settings for the clarified images are listed in Table 4.1.

Figure 4.7 shows images using the various parameter settings. The top row consists of the unaltered images with a 1% brightness threshold applied. The middle row consists of the clarified images, also at a threshold of 1%. The bottom row consists of

Table 4.1: Image Processing Parameter Settings for Clarified Images

	Baseline	Clarified
Contrast	1.0	1.22
$\gamma$	1.0	2.04
Saturation	0	24
Blue	1.0	3.162

the unaltered images with a 5% brightness threshold applied.

A number of trends are immediately apparent. The clarified color image is much clearer than the unaltered image; the chemiluminescence is much more visible to the naked eye. Among the thresholded images, since the initial image is brighter, the clarified thresholded image has more white pixels than its unaltered counterpart. Similarly, since the threshold is higher, the 5% threshold image has less white pixels than the unaltered image. Note that the edge shape is fairly consistent, and that the key difference in these images comes from the number of internal pixels. In the edge front images, the general shape is similar between all three images, though the 5% threshold image loses some of the overall outline. The unaltered and the clarified images are nearly identical, only losing some of the inner wrinkling.

Figure 4.8 shows the imaging cycle data for both  $V_I$  and  $V_{II}$  with the parameter alterations.

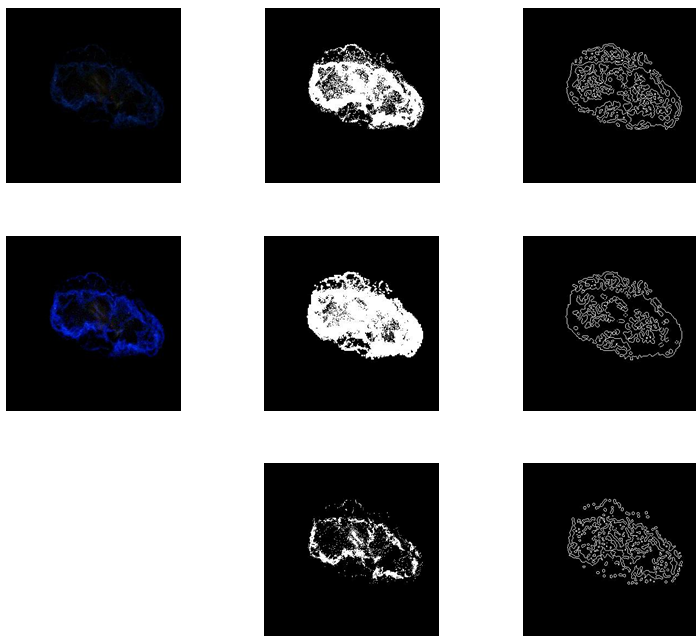


Figure 4.7: Images with different parameter processing. The top row consists of the unaltered images; the middle row, the clarified images; the bottom row, the 5% threshold images.

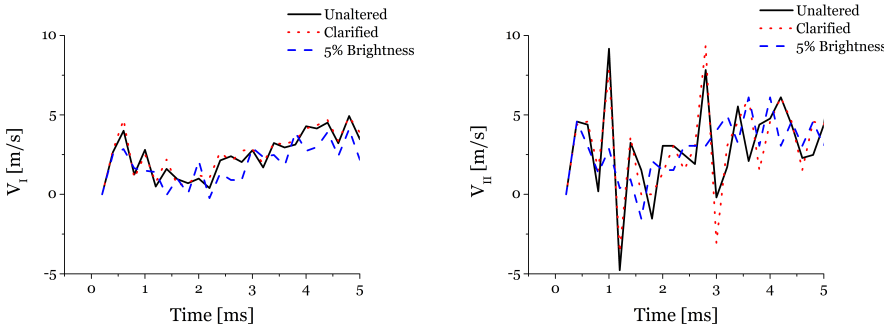


Figure 4.8: Flame speed data for modified images.

The  $V_I$  data agree very well, maintaining values within 15% of the unaltered values. In particular, the difference between the unaltered and clarified images are small, even though the original color images are quite different. For  $V_{II}$ , the changes between the unaltered and modified images are more striking, some values in close agreement while others can differ by a factor of two.  $V_{II}$  is clearly much more sensitive to the image processing than  $V_I$ . By losing the detail from the color image with the 5% threshold, the area image lacks pixels but maintains a similar edge profile. Consequently, the data derived from the 5% brightness threshold do not exhibit as much noise as the other image settings.

# Chapter 5

## Imaging Results

Using the methods described in the previous chapter, quantitative and qualitative analyses of imaging and engine data characterize the in-cylinder ignition and combustion event during HCCI and SA HCCI engine operation. The results of the engine metrics were presented earlier. The results of the imaging studies are presented here..

### 5.1 Apparatus Settings for Imaging Study

The following sections describe the SCORE and camera settings used in the imaging study. These setting were chosen to match conditions that were previously studied exclusively for emissions

in order to examine imaging trends between the data and the emissions and other engine performance metrics.

### 5.1.1 SCORE Settings

The goal of the study was to examine stable HCCI and SA HCCI conditions, so the SCORE settings were chosen to match previous experiments that were stable and represented different types of ignition and combustion modes. The preheat temperature was 320°C, which is sufficient for stable HCCI combustion at most equivalence ratios while allowing spark assistance to have meaningful effect, as seen in the metal piston emission studies. The oil temperature was 60°C, and the coolant temperature was 90°C. A constant speed of 700 RPM was maintained throughout all experiments. Indolene fuel was exclusively used for all experiments.

### 5.1.2 Camera Settings

The Vision Research camera settings were similar to previous SCORE work [10, 25]. Images were captured at 3000 frames per second (fps) for a period of about 9 seconds (roughly 27,800 frames). This limit is due to the memory capacity of the camera, which is about 3 gigabytes. The exposure time was 309  $\mu$ s. The resolution of each image was 320 x 320, sufficient to capture the



entire viewing area of the combustion chamber. The captured images were saved as .cine files before processing.

### 5.1.3 Image Processing

The .cine files were converted into .jpg files without enhancement. Gamma, RGB, contrast and brightness values remained unaltered to preserve consistency between the experiments; the baseline settings can be found in Table 4.1. The individual files were then processed using the methods described in the previous chapter with a 1% brightness threshold.  $V_I$  and  $V_{II}$  were then calculated.

## 5.2 Experimental Results

### 5.2.1 Experimental Settings

Three equivalence ratio targets were chosen to provide a range of combustion conditions ranging from strong HCCI to the lean limit of the SCORE's operation. At each equivalence ratio, three spark timings were examined: unassisted HCCI, 20° BTDC, and 40° BTDC. This range shows the stability of HCCI and the potential effects of spark assistance and changes within spark timing. The conditions for these nine experiments are summarized

in Table 5.1.

<b>Experiment</b>	$\phi$	<b>Spark Assist [° BTDC]</b>
R0	0.58	-
R20	0.59	20
R40	0.58	40
M0	0.52	-
M20	0.51	20
M40	0.51	40
L0	0.46	-
L20	0.44	20
L40	0.45	40

Table 5.1: Experimental conditions for imaging study. Experiments are listed by equivalence ratio, ranging from rich to lean.

Experiments R0-40, with the highest equivalence ratios, represent strong HCCI and attempts to control it with spark timing. Strong HCCI conditions tend to yield high levels of  $\text{NO}_x$  and high peak pressures. Experiments M0-40 represent stable HCCI at a middle range of equivalence ratio. These conditions tend to yield low levels of  $\text{NO}_x$  and power comparable to SI. Namely, these are the most desirable conditions in HCCI studies. Experiments L0-40 approach the lean limit of the SCORE's ability to operate. These conditions were chosen to examine marginal

conditions of HCCI operation and potential benefits that spark assistance can have, as shown in previous work [10, 26]. Experiments at these conditions have a tendency toward incomplete combustion or complete misfire.

Imaging, pressure, and emissions data were collected for each condition. The engine metrics considered most important for this study were maximum cylinder pressure ( $P_{\max}$ ), phasing of maximum cylinder pressure ( $\theta_{P_{\max}}$ ), maximum heat release rate ( $\text{HRR}_{\max}$ ), and indicated mean effective pressure (IMEP). Table 5.2 below shows data averaged over 27 cycles for each experiment based on the in-cylinder pressure data and the emissions data. They are divided by spark timing in order to correlate better with later discussion.

Table 5.2: Engine and emissions data averaged over 27 cycles

<b>Expt.</b>	<b>NO<sub>x</sub></b> <b>[ppm]</b>	<b>HC</b> <b>[ppm]</b>	<b>CO</b> <b>[%]</b>	<b>P<sub>max</sub></b> <b>[bar]</b>	<b>θ<sub>P<sub>max</sub></sub></b> <b>[° ATDC]</b>	<b>HRR<sub>max</sub></b> <b>[J/CAD]</b>	<b>IMEP</b> <b>[bar]</b>
R0	2139	263	0.08	29.8	-6.19	63.2	0.310
M0	21	514	0.15	25.4	3.10	24.8	0.607
L0	13	647	0.18	19.8	8.24	10.3	0.613
R20	2440	226	0.08	29.7	-6.60	64.1	0.230
M20	40	443	0.13	26.1	1.47	27.0	0.513
L20	25	645	0.17	21.5	5.88	13.2	0.642
R40	2839	216	0.08	29.8	-6.74	56.6	0.155
M40	145	348	0.13	27.4	-3.46	30.4	0.350
L40	11	670	0.17	20.6	5.96	10.8	0.534

## 5.2.2 Equivalence Ratio Effects

The following sections examine changes in equivalence ratio within a single spark timing and the resulting effects on imaging data, engine metrics, and emissions.

### 5.2.2.1 Unassisted HCCI

Experiments R0, M0, and L0 were all operated under unassisted auto-ignition conditions. Figure 5.1 shows the corresponding propagation rate  $V_I$  and the heat release rate as function of CAD. For these experiments,  $V_I$  indicates the rate of the chemiluminescence filling the viewing area due to autoignition.

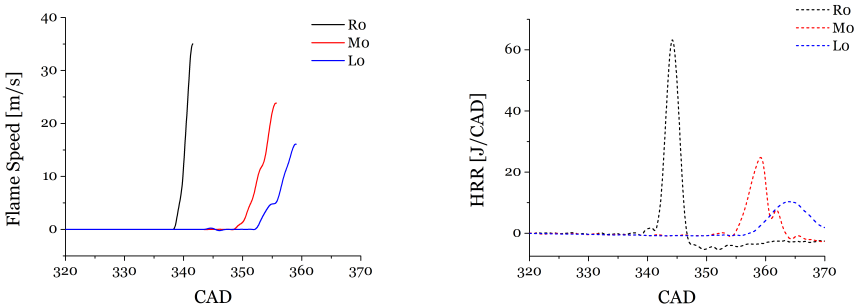


Figure 5.1:  $V_I$  and HRR data for unassisted HCCI experiments

The imaging cycles were synchronized using the pressure data. The CAD at which peak intensity occurred was defined by the

maximum rate of pressure rise. Between these peaks, 720 CAD were evenly distributed, resulting in the CAD-resolved imaging data seen in the figures in this chapter.

For each operating condition, the chemiluminescence rapidly fills the viewing area, yielding propagation rates consistently in excess of 10 m/s. The decrease in  $V_I$  after the maximum is an artifact of the image processing; the reaction fronts do not decrease in propagation rate. Figure 5.1 shows that the propagation rates follow trends that are consistent with the heat release rate.

Experiment R0, the richest case, had a very high peak heat release rate (63.2 J/CAD) and very early phasing of peak pressure ( $-6.19^\circ$  atdc). Based on these parameters alone and the discussion in the previous chapters, this experiment should yield high  $\text{NO}_x$  values, and it does (2139 ppm). Despite the high equivalence ratio and heat release rate, the early phasing causes the IMEP to be rather low, only 0.310 bar. Like the heat release rate, the propagation rate rises abruptly and reaches its maximum very quickly.

Experiment M0, the midrange case, has a lower heat release rate that is more distributed in time and later in phasing. This distribution of the heat release and the delay of the phasing result in significantly lower  $\text{NO}_x$  emissions (21 ppm). The later phasing also increases the IMEP to 0.607 bar despite the more lean

condition. The  $V_I$  data also follow this trend, being distributed over a longer period of time as seen in Figure 5.1.

Experiment L0, the most lean case, has the lowest heat release rate which is distributed over the longest period of time. The phasing is the latest of the unassisted experiments, resulting in low  $\text{NO}_x$  (13 ppm) and IMEP (0.613 bar) comparable to experiment M0 despite having a lower equivalence ratio and lower peak pressure. The imaging data show the chemiluminescence still begins abruptly, and the rise is distributed over the longest time compared to M0 and R0.

### 5.2.2.2 20° BTDC Spark Assist

Experiments R20, M20, and L20 were operated with spark assist at 20° BTDC. Figure 5.2 shows the flame speed  $V_{II}$  and HRR data. Again, the general trends are consistent between the heat release rate and the propagation rates for  $V_{II}$ . The addition of the spark assist is slightly evident at 340 CAD, where there is a rise in the propagation rate that correlates with the initial visibility of the spark plasma. The drop after this initial rise comes from the spark plasma retracting, which is interpreted as a negative flame speed. This is more evident in experiments M20 and L20.

Experiment R20, the richest case, is very similar to experiment R0. Both have high HRR ( $> 60 \text{ J/CAD}$ ), early phasing of peak

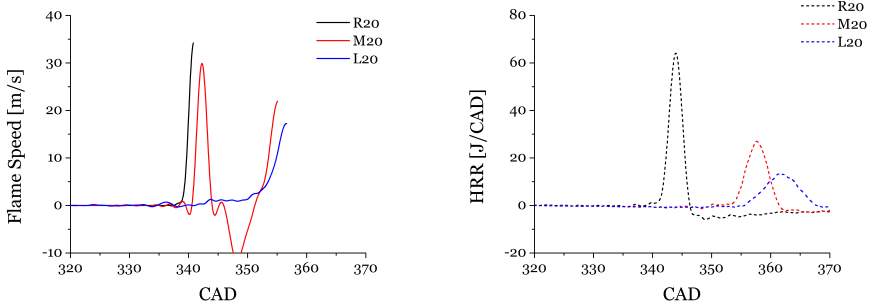


Figure 5.2:  $V_{II}$  and HRR data for  $20^\circ$  BTDC spark assist experiments

pressure ( $\sim 6^\circ$  BTDC), high  $\text{NO}_x$  values ( $> 2000$  ppm), and low IMEP ( $< 0.3$  bar). The imaging data show that the spark had little to no effect on ignition and combustion, as autoignition occurred at the same phasing with or without the spark plasma and no flame propagation was observed. The spark plasma was not a significant source of ignition and flame propagation at these conditions.

Experiment M20 starts to show the effects of spark assistance. The spark plasma was not always visible in the imaging data. The data for  $V_{II}$ , however, show a sharp increase at 340 CAD, followed by a slow rise from 1–4 m/s as the flame propagates throughout the chamber. Autoignition occurs later (that is, the phasing retards to after TDC), which produces lower  $\text{NO}_x$  and

higher IMEP. Peak pressure and peak HRR decrease as well, which is expected from the decrease in equivalence ratio. Overall, this is a stable SA HCCI operating condition.

Experiment L20 continues many of the trends shown in experiment M20. The plasma is evident, and the flame speed slowly increases from 1–4 m/s until autoignition. Peak pressure and HRR decrease, but the phasing retards to about  $6^\circ$  ATDC, resulting in low  $\text{NO}_x$  and higher IMEP than both R20 and M20. This condition is a good example of low-load SA HCCI operation. Despite the lower equivalence ratio, the engine power and efficiency is better than the rich conditions due to the later ignition phasing advanced by SA HCCI.

### 5.2.2.3 $40^\circ$ BTDC Spark Assist

Experiments R40, M40, and L40 were all operated with spark assist at  $40^\circ$  BTDC. Figure 5.3 shows the corresponding data for  $V_{II}$  and HRR. Figure 5.3 presents  $V_{II}$  as a function of CAD where the scale focuss on the early time after spark. The effects of spark assist are much more evident here, particularly in the imaging data.

Experiment R40 had the highest peak pressure, HRR, and  $\text{NO}_x$  levels, the lowest IMEP, and most advanced phasing of peak pressure, all comparable to experiments R0 and R20. Of note is that the



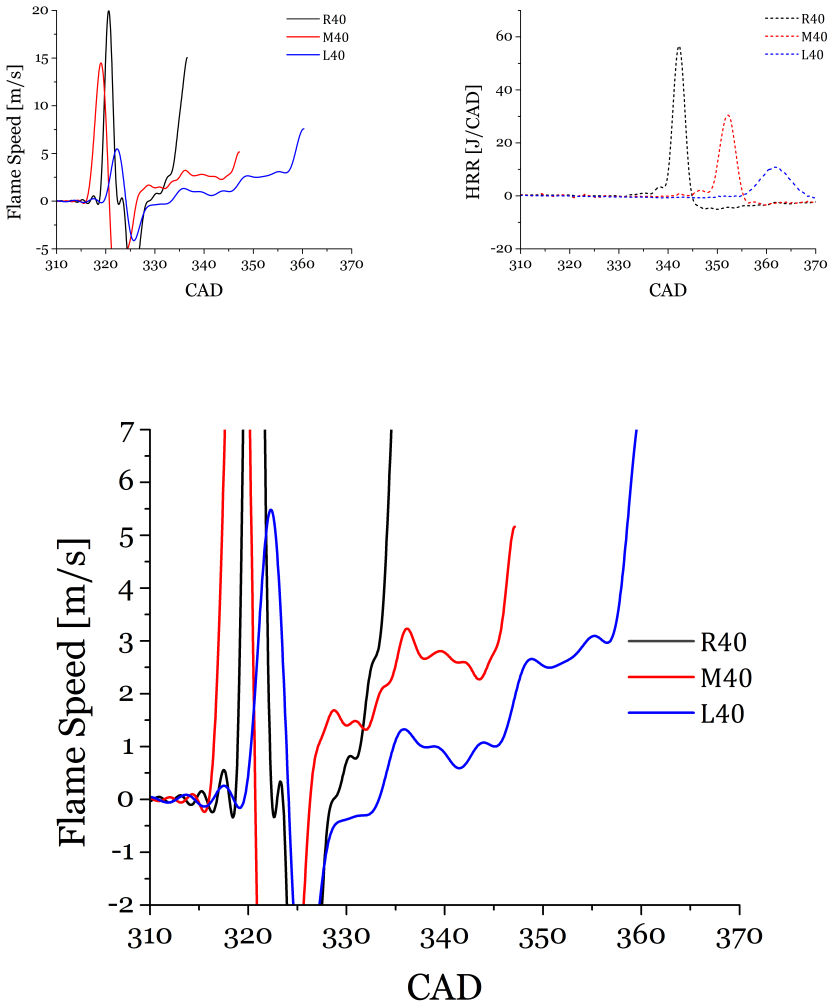


Figure 5.3:  $V_{II}$  and HRR data for 40° BTDC spark assist experiments. Bottom image included to clarify flame propagation.

spark ignition of a flame at 320 CAD is more evident. The flame slowly propagates until around 340 CAD, when autoignition occurs.

Experiment M40 shows more the effects of spark assistance. The spark plasma is visible at 320 CAD, and then the flame propagation rate steadily increases until autoignition occurs at around 350 CAD. Throughout the flame propagation, the HRR remains near zero; the majority of the heat release occurs during autoignition, which starts right before 350 CAD. By decreasing the equivalence ratio, the spark assist starts to have a greater effect, and the phasing retards, resulting in lower  $\text{NO}_x$  and higher IMEP. Peak pressure and HRR decrease as well. Of note is that since the phasing is still early ( $-3.46^\circ$  ATDC), the  $\text{NO}_x$  levels are higher than the other midrange and lean experiments, and the IMEP is the lowest of these experiments. While this is still a stable SA HCCI condition, it is not optimal.

Experiment L40 continues many of the trends from experiment M40 derived from the change in equivalence ratio. Phasing retards to after TDC, producing low  $\text{NO}_x$  and higher IMEP. Peak pressure and HRR decrease further. While the autoignition happens slightly later, the spark ignition occurs at 320 CAD, identical to the other two experiments, and the increase in the flame propagation rate is similar to that of M40, increasing from 1–4

m/s before autoignition. Since autoignition starts later in L40, the acceleration of this flame propagation is slower than in M40. Again, the majority of the heat release does not occur during flame propagation, but rather during autoignition. These conditions exhibit clear features of both Regimes I and II. Ultimately, this is the most stable SA HCCI condition at this spark timing.

### 5.2.3 Spark Timing Effects

This section examines the effects of advancing spark assist while maintaining a constant equivalence ratio. Table 5.3 shows the same engine and emissions data, but grouped by equivalence ratio instead of spark timing. Six additional experiments were performed to expand the spark timing range for the midrange and lean conditions; the spark timings were 30, 50, and 60° BTDC.

#### 5.2.3.1 Rich Equivalence Ratio Conditions

Figure 5.4 shows the flame propagation rate and HRR data for the three richest conditions, with an equivalence ratio of about  $\phi = 0.6$ .

The imaging data for the rich conditions were quite similar regardless of the spark timing. All had autoignition occurring at around 340 CAD, and all yielded HRRs which were quite rapid, spanning less than 10 CAD. For R20, there is almost no evidence

Table 5.3: Engine and emissions data averaged over 27 cycles.

Expt.	$\phi$	$\text{NO}_x$ [ppm]	HC [ppm]	CO [%]	$P_{\max}$ [bar]	$\theta_{P_{\max}}$ [ $^\circ$ ATDC]	$\text{HRR}_{\max}$ [J/CAD]	IMEP [bar]
R0	0.58	2139	263	0.08	29.8	-6.19	63.2	0.310
R20	0.59	2440	226	0.08	29.7	-6.60	64.1	0.230
R40	0.58	2839	216	0.08	29.8	-6.74	56.6	0.155
M0	0.52	21	514	0.15	25.4	3.10	24.8	0.607
M20	0.51	40	443	0.13	26.1	1.47	27.0	0.513
M30	0.53	58	415	0.17	27.3	-1.86	31.6	0.770
M40	0.51	145	348	0.13	27.4	-3.46	30.4	0.350
M50	0.53	327	320	0.12	28.8	-4.98	32.8	0.446
M60	0.53	520	313	0.14	27.6	-6.23	26.9	0.448
L0	0.46	13	647	0.18	19.8	8.24	10.3	0.613
L20	0.45	25	645	0.17	21.5	5.88	13.2	0.642
L30	0.45	21	588	0.16	24.2	2.48	18.0	0.354
L40	0.45	11	670	0.17	20.6	5.96	10.8	0.534
L50	0.45	3	538	0.13	24.5	1.20	16.2	0.256
L60	0.45	7	616	0.16	23.6	2.04	13.7	0.612

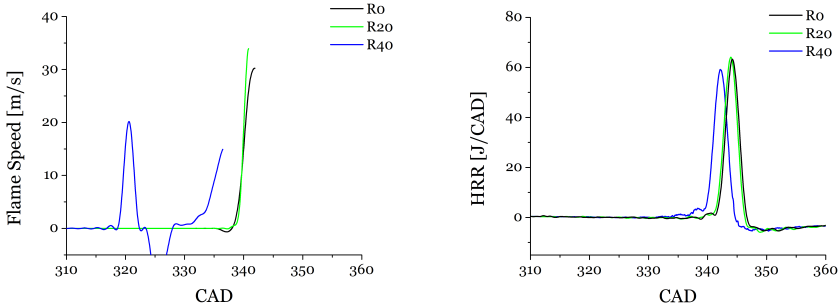


Figure 5.4: Flame propagation rate and HRR data for experiments R0, R20, and R40.

of the spark plasma in the imaging data, one cycle excepting. While it may seem that the spark plasma is initiating the autoignition, this is not the case. Kernels of ignition form while the plasma is still present, as seen in Figure 5.5. Note the pockets of ignition in the second frame which have already formed before spark ignition, and how in the next two frames, the autoignition is clearly occurring while the spark plasma is forming, indicating that the spark plasma does not aid autoignition. In R40, the spark plasma is well captured in the imaging data, leading to a flame formation and slight increase in flame speed from 1–4 m/s until autoignition occurs. In all cases, autoignition is the dominant mode of reaction, but flame propagation starts to be more apparent in the more advanced spark assist timings.

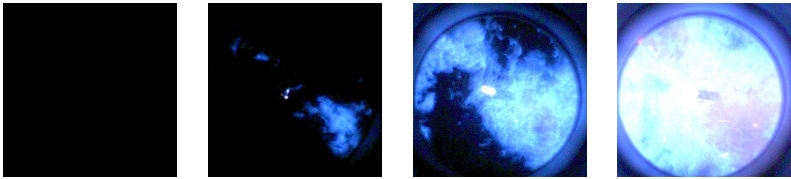


Figure 5.5: Sequential images from a representative cycle from experiment R20.

The heat release rate data for the rich conditions were also quite similar. All experiments had high heat release rates ( $> 60$  J/CAD) occurring well before top dead center ( $> 6^\circ$  BTDC). The magnitude changes slightly with advancing spark timing, with R0 and R20 having comparable values and R40 having the

lowest, potentially indicating that while the flame propagation does not contribute significantly to the overall heat release time history, there may be a slight effect on the peak heat release. For this equivalence ratio, the only significant effects that the spark assistance seems to have are to lower the IMEP and to raise  $\text{NO}_x$ . Overall, spark assist does not affect combustion significantly at such strong HCCI conditions.

### 5.2.3.2 Midrange Equivalence Ratio Conditions

The experiments labeled M have a midrange equivalence ratio of about  $\phi = 0.5$ , more suited to stable HCCI operation. Figure 5.6 shows the flame velocity and HRR data for these experiments.

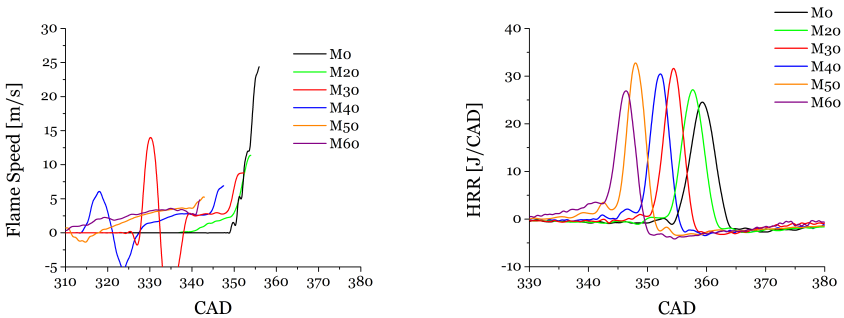


Figure 5.6: Flame propagation rate and HRR data for midrange equivalence ratio conditions.

Spark assistance had a much greater effect on these experiments.

The imaging data show the steady increase in flame velocity until autoignition. Of note is that the spark plasma is not evident in the imaging data for the earliest spark timings (L50-60) despite a clear flame front forming. This is potentially explained by the fact that the plasma is not as luminescent compared to its surroundings, limiting the sharp velocity change evident in some of the later spark timings, e.g. M30.

Advancing the spark timing from 20 to 60° BTDC causes the autoignition to occur earlier. The spark plasma is clearly initiating a flame front that propagates throughout the combustion chamber. Earlier initiation of this front induces earlier autoignition, up to a point. For the M50 and M60 experiments, autoignition seems to start at the same time, indicating that there is a limit to which spark assist can produce a flame front.

The heat release data follow a similar trend. Advancing spark assistance causes autoignition to occur earlier, and thus the heat release starts earlier as well. Of note is that the magnitude increases with advancing spark assistance until M50. While the flame propagation does not contribute much to the heat release, the fact that it induces earlier autoignition causes an increase in HRR. The peak pressure also increases slightly with advancing spark, a trend not seen in the rich conditions. Of importance is that the phasing of peak pressure changes dramatically with

advancing spark assistance, ranging from a few degrees after top dead center (M0), to a few degrees before top dead center (M30-60). As a result, IMEP decreases and  $\text{NO}_x$  increases with advancing spark timing. Starting with M30, the combustion seems to approach a regime of “strong” SA HCCI, where the spark assist advances the phasing enough to induce high  $\text{NO}_x$ . Previous emission studies, shown in chapter 3, have investigated this phenomenon, where a normally stable, low emission HCCI or SA HCCI condition transitions into a condition with high levels of  $\text{NO}_x$  [26]. Overall, it seems that this stable HCCI condition is not adversely affected by the  $20^\circ$  BTDC spark assistance, but advancing spark timing further could induce effects in opposition to those desired from HCCI operation.

### 5.2.3.3 Lean Equivalence Ratio Conditions

The lean conditions, with an equivalence ratio of about  $\phi = 0.45$ , show the effects of spark assistance on low-load HCCI operation. Figure 5.7 shows the flame propagation rate and HRR data.

While the midrange experiments exhibited a steady increase in flame speed before autoignition, the lean experiments have a slightly different trend. For L20, the flame speed is very low ( $< 1$  m/s) until autoignition, indicating that the flame propagation, while present, is not nearly as strong. Like the midrange



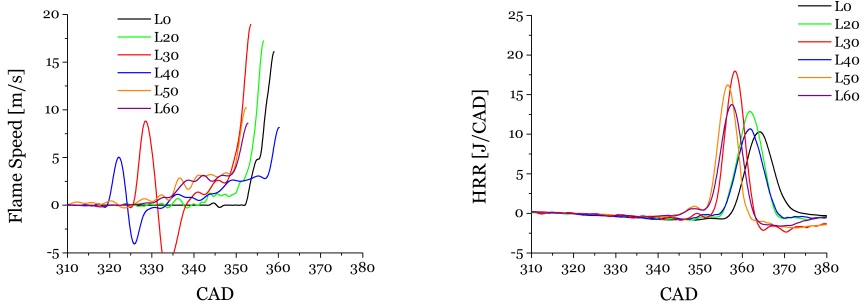


Figure 5.7: Flame propagation rate and HRR data for lean equivalence ratio conditions.

conditions, the spark plasma is only evident in the L30 and L40 conditions; the luminosity of the plasma is highest compared to the surroundings at these conditions. For L30 and L40, the flame speed slowly increases from 1–4 m/s until autoignition. The earliest spark timings (L50 and L60) exhibit behavior not seen in any other experiment. The flame front starts off extremely slow, less than 1 m/s, until about 330 CAD, when it rises to about 2–3 m/s. Unlike the other experiments, the flame speed does not accelerate further; it remains relatively constant until autoignition.

Emissions for all of these experiments are similar, having  $\text{NO}_x$  values well below 50 ppm and HC values from 500–700 ppm; these are comparable to weak HCCI and weak SA HCCI conditions.

Peak pressures are comparable as well, but the phasing is different. This is expected from spark assist, but the phasing does not monotonically advance. L0 has phasing of about  $8^\circ$  ATDC, while the spark assist experiments have phasing ranging from  $1-6^\circ$  ATDC. Notably, the phasing of L40 is later than that of L30 by about 3 degrees, despite initiating spark 10 degrees earlier. Consequently, IMEP for L40 is higher than that for L30. The variance in the phasing may come from the lean nature of the combustion. The autoignition is weakest at this equivalence ratio, so flame propagation can have more drastic effects than merely shifting the phasing of autoignition. The heat release rate data further support these trends. The duration of the heat release is comparable for each spark timing, but the magnitude is slightly higher for the earlier phasing.

### 5.3 Estimates for In-Cylinder Temperature

Since HCCI is controlled by chemical kinetics, and temperature is the chief parameter for reactivity, an understanding of the transient in-cylinder temperature provides insight into the fundamental behavior of HCCI. Temperature cannot be measured directly with the current SCORE setup, but it can be estimated using thermodynamic relations and the in-cylinder

pressure measurement.

### 5.3.1 Temperature Estimation Algorithm

The method by which temperature is estimated was derived by Mohammad Fatouraie in the Combustion and Environmental Research Laboratory (CERL) at the University of Michigan. It captures the isentropic compression temperature change, accounting for the gamma effects of the different fuel/air mixtures. Using the instantaneous pressure, global fuel/air mixture, and ideal gas relations, the instantaneous in-cylinder temperature is calculated.

The algorithm cannot account for combustion, so temperature values are limited to about 1200 K. The temperature information prior to this maximum can indicate the reasons for the observations of flame propagation and autoignition.

### 5.3.2 Midrange Condition Temperatures

Figure 5.8 shows the temperature profiles for the midrange conditions. The HCCI condition (M0) compresses isentropically until about TDC when autoignition starts. Adding spark assist advances the temperature increase slightly, similar to the flame speed trends. Notably, the temperature profiles for the later spark timings M20–M40 are nearly identical until about CAD

340, when M30 and M40 start rising faster than M20 and M0. This is consistent with the flame speed measurements; at this point, M30 and M40 are well into autoignition, while M20 and M0 have little to no visible flame. The two earliest spark timing experiments (M50 and M60) start to deviate from M0 around CAD 330, again well into flame propagation. Of note is that while the heat release for flame propagation is minimal, the temperature rise relative to the unassisted case is markedly different. Also of note is that the flame propagation does not significantly affect the temperature rise until 20–30 CAD after the spark initiates; the fact that M50 and M60 do not have significant temperature rise until 30° BTDC shows that the initial flames do not raise global temperatures appreciably.

### 5.3.3 Lean Condition Temperatures

Figure 5.9 shows the temperature profile for the lean conditions. Similar to the midrange conditions, advanced spark timing advances temperature rise. L20 and L40 have very similar temperature traces, with flame propagation starting a slight temperature rise around CAD 345 and autoignition occurring around CAD 355. L30, L50, and L60 are also similar, with a slight temperature rise around CAD 335 and autoignition around CAD 350. These overall trends are very similar to the flame speed trends, with L30 having earlier phasing than L40.

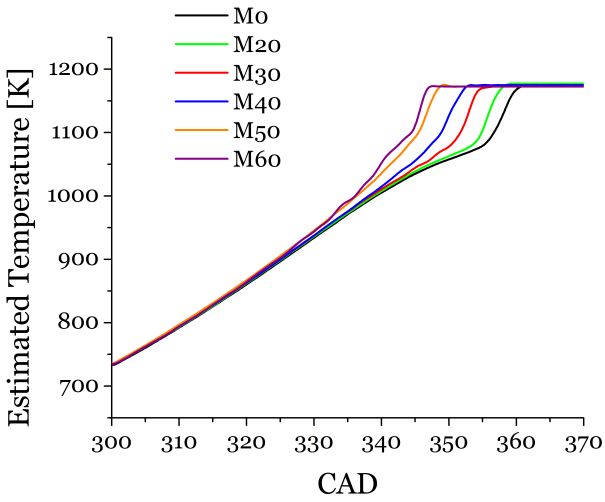


Figure 5.8: Temperature profile for midrange conditions.

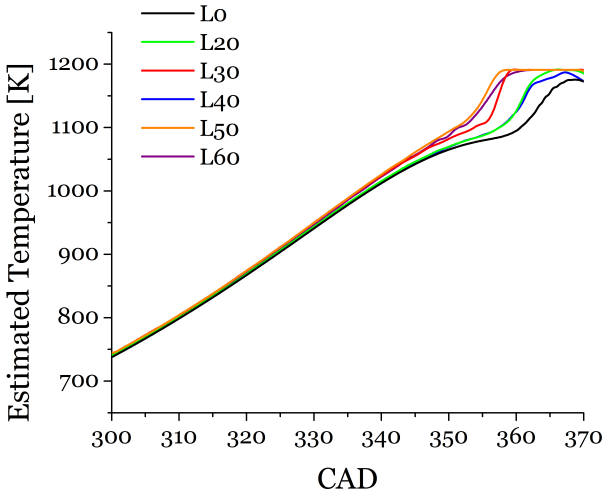


Figure 5.9: Temperature profile for lean conditions.

The temperature change is evident in the flame speed data, an example of which can be seen in Figure 5.10. Three conditions were chosen to simplify the figure, but the trends are evident at both the midrange and lean conditions. With advancing spark comes earlier flame propagation, evident in the flame speed profile, and a rise in temperature, evident in the temperature profile. The earlier phasing of autoignition is also evident in both profiles. Most notably, the early flame propagation of M60 initiates a slight temperature rise compared to the M40 and M0 cases.

### 5.3.4 Estimated Autoignition Temperature Comparison

The estimated autoignition temperature of the previous experiments was calculated using the Fatouraie algorithm and tabulated in Table 5.4.

Table 5.4: Estimated autoignition temperatures of midrange and lean engine conditions.

<b>Condition</b>	$T_{ign}$ [K]	<b>Condition</b>	$T_{ign}$ [K]
M0	1057	L0	1077
M20	1058	L20	1080
M30	1054	L30	1077
M40	1066	L40	1081
M50	1060	L50	1094
M60	1076	L60	1098
Midrange Average	1062	Lean Average	1084

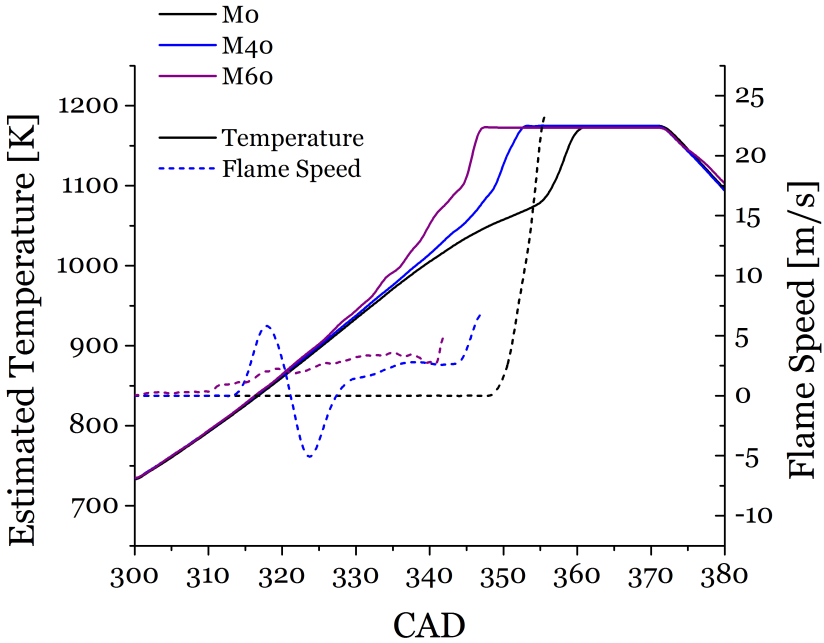


Figure 5.10: Temperature and velocity profiles for selected midrange conditions



## 5.4 Comparison to Detailed Image Analysis

Much of the purpose of this study is to investigate the new image processing methods (hereto referred as the “Keros methods”) and what information they can provide. These methods take some liberties in the processing of the flame image for speed and ease. Here, the new methods are compared to other traditional and alternate image analysis approaches.

### 5.4.1 Manual Image Analysis

Kate Helleburg investigated imaging of SA HCCI combustion using a more traditional method [27]. She manually measured flame velocities along eight cardinal directions ( $45^\circ$  incremental divisions of a circle), as seen in Figure 5.11 below. Using the spark plasma as the center of her analysis, flame locations were measured for each individual frame and then converted into instantaneous flame speeds. These were compiled and averaged to produce plots similar to Figure 5.11.

The measurements were taken manually for about 13 representative cycles from 6 engine conditions from Brad Zigler’s data [10, 28]. The manual image processing allowed for flame speed measurements in a number of directions, giving spatial resolution that the thresholding methods do not have [27]. One sample

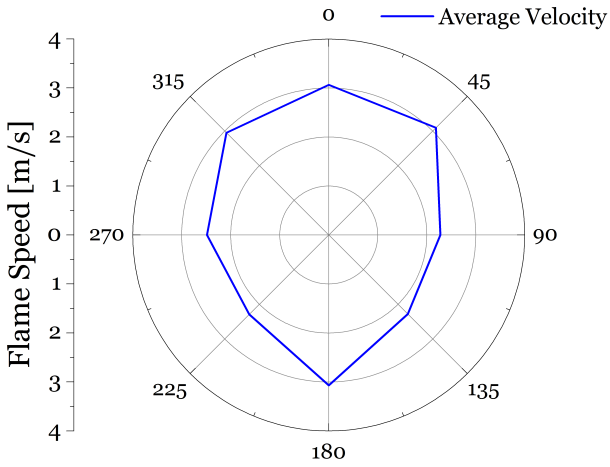


Figure 5.11: Average cardinal velocity diagram.

flame front profile is shown in Figure 5.12. For each cycle, the CAD was determined using the engine speed and spark timing, and the location of the flame front at each of the eight cardinal directions was measured. These measurements were then superimposed for each frame, giving a plot similar to the one in Figure 5.12.

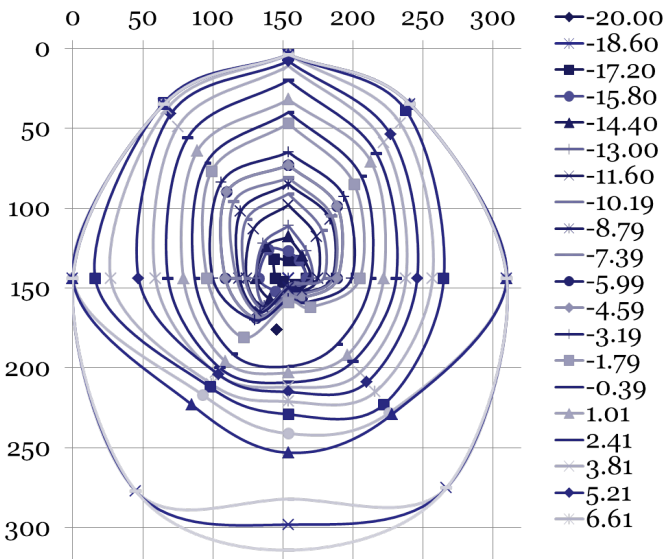


Figure 5.12: Framewise cardinal flame front diagram.  $T_{in} = 271^{\circ}\text{C}$ ,  $\phi = 0.45$ , SA20.

While the flame image is not always perfectly circular, the directional velocities range from about 1–4 m/s before autoignition; as seen in Figure 5.13, there is no particular trend in any di-

rection. Averaging around the cardinal points, the flame speed rises from 1–4 m/s before autoignition [27]. This is comparable to the  $V_{II}$  measurements of the current work. Looking at the average velocity across the 13 cycles, as in Figure 5.14, there is a rise from about 1–4 m/s before autoignition, again similar to  $V_{II}$  measurements. Overall, while the thresholding methods do not capture the spatial variation of the manual method, the average flame speed trends of the thresholding are comparable.

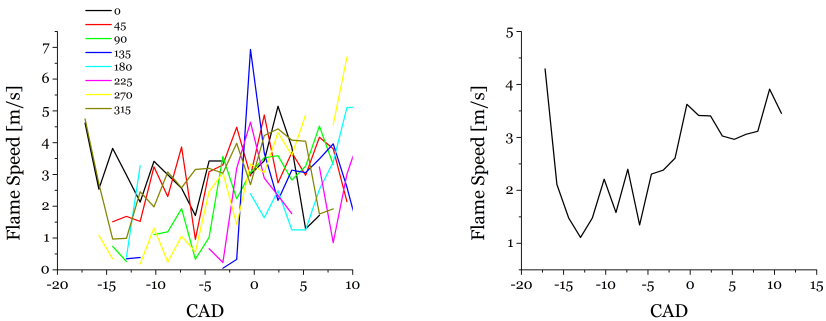


Figure 5.13: Cardinal and average velocity measurements.

#### 5.4.2 Spatial Resolution of Edge Front Method

In the calculation of the edge front velocity ( $V_{II}$ ), there is some spatial resolution recognized. The vertical and horizontal lengths are averaged for a representative edge. The question naturally arises whether this average is a reasonable approximation, and

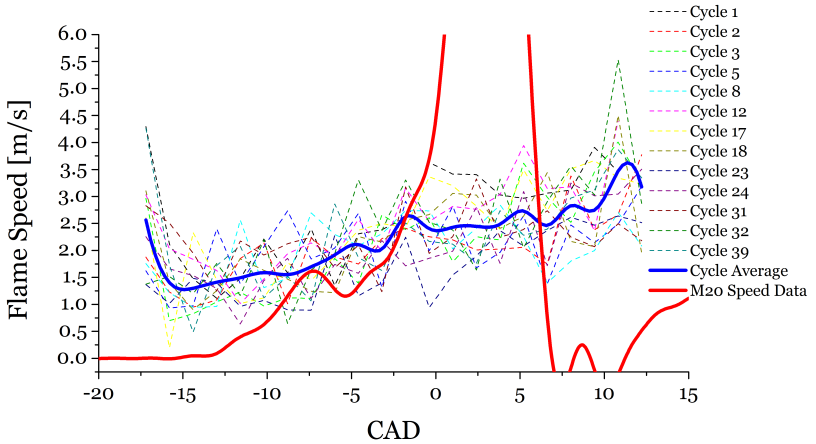


Figure 5.14: Average velocities for all cycles.

this section examines the differences between the vertical and horizontal lengths in the  $V_{II}$  calculation.

Dimensional measurements from experiment L40 were examined to investigate the differences in the orthogonal velocity. The results of this analysis can be seen in Figure 5.15. The lengths in the  $X$  and  $Y$  directions and the difference between the two are plotted. The difference was also normalized to the maximum dimension of 0.05 m:

The normalized length difference starts near 0, rising to about 0.25 near autoignition. During the main flame propagation, the

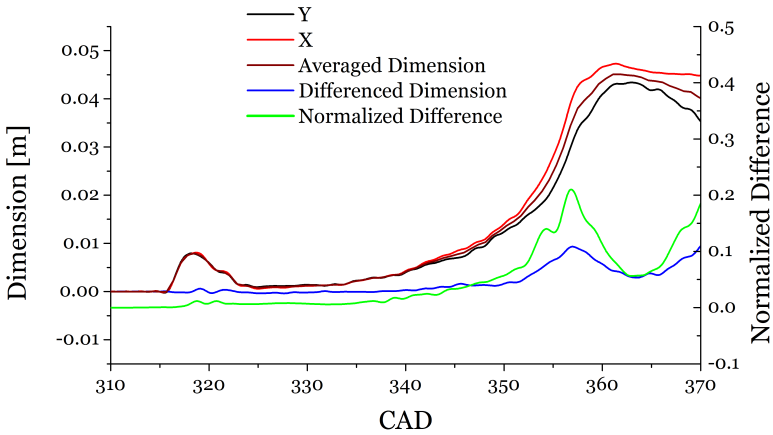


Figure 5.15: Directional dimensions compared to  $V_{II}$  for L40.

normalized difference is at most 10%. The data show the flame propagation is approximately isotropic, and averaging the two dimensions is not biasing the data.

# Chapter 6

## Conclusions and Future Work

### 6.1 Conclusions

A series of experiments of HCCI and spark-assisted HCCI operation were conducted on the University of Michigan single-cylinder optical research engine. This section comprises the primary conclusions of the studies detailed in this investigation.

To understand the formation of emissions in HCCI and SA HCCI, a wide range of engine conditions were investigated, acquiring in-cylinder pressure data, emissions measurements, and high speed in-cylinder imaging data. Intake temperature variations of 280 – 360°C, equivalence ratio ranges from 0.4–0.6, and spark timings from 10–70° BTDC allowed for conditions of HCCI and SA HCCI that exhibited one of three general

characteristics: strong, high emission combustion; stable, low emission combustion; or weak, unstable combustion. The study found that the phasing of peak pressure is an excellent metric for  $\text{NO}_x$  formation, with experiments whose phasing is before TDC (often  $5\text{--}10^\circ$  BTDC) having high  $\text{NO}_x$  ( $> 1000$  ppm), while phasing after TDC (especially  $2^\circ$  ATDC and later) has low  $\text{NO}_x$  ( $< 100$  ppm for  $2^\circ$  ATDC and later). Similarly, there is a  $\text{NO}_x$ –HC tradeoff; as  $\text{NO}_x$  decreases (often from 2000 ppm to less than 100 ppm), HC increases from about 300 ppm to about 800 ppm.

To analyze optical data from the engine, two new image processing methods were developed, designed based on the features of the autoignition and flame propagation regimes. Thresholding was used to convert color images into binary black and white images. The autoignition method converts the image to an equivalent disc, the radius of which is measured to find  $V_I$ . The front propagation method applies an edge front algorithm that returns a 1-pixel width trace of the image. The orthogonal dimensions of this trace are measured, the average becoming the diameter of an equivalent circle. The change in the radius of this equivalent circle is used to find  $V_{II}$ .

These methods were then applied to a set of engine experiments investigating spark timing effects of stable and unsta-



ble SA HCCI. From the imaging data, the spark initiates flame propagation with flame speed increasing from 1-4 m/s until autoignition occurs. Spark assist can be used to shift ignition phasing under certain conditions. For fast HCCI chemistry, usually with high preheat and equivalence ratio, flame propagation is too slow compared to autoignition, so the spark does not significantly affect combustion. At these conditions, partial stratification may help to adjust the chemistry speed. For slow HCCI chemistry, there is sufficient time for flame propagation to occur, so phasing can be advanced with spark assist. Compared to traditional manual image processing, the new methods have comparable flame speed calculations. The flame speed data are useful metrics for characterizing SA HCCI operation.

## 6.2 Future Work

As extensive as the present study has been, there is plenty of opportunity for further investigation. The current imaging methods can be applied to higher speed and load conditions. Stratified charge compression ignition could be investigated in addition to HCCI, similar to the gasoline direct injection engines in modern market vehicles. Different fuel blends can be used, particularly low-octane fuels or biofuel blends that are starting to become

more common.

The image processing methods themselves can be further refined. Directional variation can be measured to account for the eccentricities of the flame front. Differing thresholds can be used to identify segments of the flame; in particular, one threshold could be used for the initial autoignition site (such as the spark plasma), while another threshold could be used for the subsequent propagation and autoignition. The edge front algorithm can be further refined to provide a more accurate circumscription based on the flame perimeter length.

This fundamental investigation of low temperature combustion serves as part of the ongoing effort to address modern energy issues. Applying incremental advances to existing technologies can effect positive environmental changes. This work is a response to the ubiquitous challenge imposed on engineers, scientists, and all who strive for a sustainable existence.

# Appendices

# Appendix A

## Engine Experimental Data

### A.1 Experimental Data Tables

Table A.1: Experimental Data - Emissions

$T_{in}$ [°C]	SA [° BTDC]	$\phi$	$NO_x$ [ppm]	HC [ppm]
262	50	0.56	180	934
274	70	0.59	2044	326
274	50	0.59	1112	343
275	20	0.55	34	545
280	20	0.57	22	658
281	30	0.52	43	845
283	50	0.59	689	431

Table A.1: Experimental Data - Emissions

<b>T<sub>in</sub></b> [°C]	<b>SA</b> [° BTDC]	$\phi$	<b>NO<sub>x</sub></b> [ppm]	<b>HC</b> [ppm]
297	20	0.60	37	547
297	50	0.59	1146	418
303	30	0.54	90	586
304	10	0.60	472	399
319	50	0.52	82	568
320	20	0.51	55	773
320	50	0.42	17	923
320	50	0.48	13	699
321	-	0.63	1713	423
321	10	0.44	25	765
321	30	0.55	77	560
324	10	0.63	1605	339
325	-	0.61	1424	335
325	-	0.49	31	651
326	-	0.40	12	876
339	-	0.64	3293	412
339	10	0.43	44	797
339	20	0.45	22	788
340	-	0.42	31	871
340	-	0.44	47	720
340	30	0.56	267	438

Table A.1: Experimental Data - Emissions

$T_{in}$ [°C]	SA [° BTDC]	$\phi$	$NO_x$ [ppm]	HC [ppm]
341	10	0.63	2639	327
342	-	0.42	8	838
359	-	0.43	32	721
360	-	0.46	22	732
361	-	0.39	37	741

Table A.2: Experimental Data - Engine Metrics

$T_{in}$ [°C]	SA [° BTDC]	$\phi$	$P_{max}$ [bar]	COV	HRR [J/CAD]	COV
262	50	0.56	32.7	0.029	27.9	0.082
274	70	0.59	33.1	0.006	33.4	0.201
274	50	0.59	33.5	0.008	39.8	0.093
275	20	0.55	25.7	0.028	20.9	0.056
280	20	0.57	28.1	0.037	25.6	0.102
281	30	0.52	22.9	0.086	14.1	0.175
283	50	0.59	34.7	0.008	38.4	0.104
297	20	0.60	29.6	0.020	30.1	0.116
297	50	0.59	35.0	0.005	47.3	0.065
303	30	0.54	30.5	0.010	33.1	0.068
304	10	0.60	33.7	0.015	52.7	0.089

Table A.2: Experimental Data - Engine Metrics

$T_{in}$ [°C]	SA [° BTDC]	$\phi$	$P_{max}$ [bar]	COV	HRR [J/CAD]	COV
319	50	0.52	31.8	0.009	31.1	0.093
320	20	0.51	25.5	0.029	19.9	0.090
320	50	0.42	20.6	0.097	9.02	0.232
320	50	0.48	28.1	0.017	21.9	0.048
321	-	0.63	35.5	0.005	73.8	0.037
321	10	0.44	23.0	0.026	14.0	0.073
321	30	0.55	31.5	0.006	37.5	0.058
324	10	0.63	35.2	0.006	70.0	0.030
325	-	0.61	33.8	0.006	67.6	0.040
325	-	0.49	26.7	0.010	26.8	0.074
326	-	0.40	20.0	0.025	10.6	0.097
339	-	0.64	34.5	0.006	81.1	0.043
339	10	0.43	25.3	0.006	18.2	0.065
339	20	0.45	23.2	0.021	14.6	0.055
340	-	0.42	20.6	0.046	9.48	0.082
340	-	0.44	26.1	0.016	20.8	0.059
340	30	0.56	32.1	0.004	44.5	0.055
341	10	0.63	34.5	0.006	73.6	0.053
342	-	0.42	20.6	0.040	11.9	0.086
359	-	0.43	24.5	0.004	16.2	0.066
360	-	0.46	25.9	0.013	20.8	0.065

Table A.2: Experimental Data - Engine Metrics

$T_{in}$ [°C]	SA [° BTDC]	$\phi$	$P_{max}$ [bar]	COV	HRR [J/CAD]	COV
361	-	0.39	22.1	0.014	9.83	0.124

Table A.3: Experimental Data - Engine Metrics

$T_{in}$ [°C]	SA [° BTDC]	$\phi$	IMEP [bar]	COV	$\theta_{P_{max}}$ [° ATDC]	COV
262	50	0.56	2.01	0.053	2.7	0.007
274	70	0.59	1.19	0.097	-5.0	0.001
274	50	0.59	1.48	0.049	-6.0	0.002
275	20	0.55	2.13	0.014	12.0	0.003
280	20	0.57	2.25	0.018	10.7	0.004
281	30	0.52	1.99	0.026	13.9	0.007
283	50	0.59	1.71	0.036	-3.2	0.002
297	20	0.60	2.24	0.007	9.6	0.002
297	50	0.59	1.71	0.029	-4.4	0.020
303	30	0.54	1.79	0.012	4.2	0.001
304	10	0.60	2.06	0.020	2.6	0.003
319	50	0.52	1.52	0.030	-0.9	0.003
320	20	0.51	1.88	0.031	11.4	0.004
320	50	0.42	1.22	0.057	11.8	0.006
320	50	0.48	1.46	0.034	4.5	0.003



Table A.3: Experimental Data - Engine Metrics

$T_{in}$ [°C]	SA [° BTDC]	$\phi$	IMEP [bar]	COV	$\theta_{P_{max}}$ [° ATDC]	COV
321	-	0.63	1.68	0.022	-5.4	0.001
321	10	0.44	1.24	0.017	9.3	0.003
321	30	0.55	1.66	0.011	1.3	0.001
324	10	0.63	1.74	0.033	-3.9	0.002
325	-	0.61	1.58	0.035	-4.1	0.002
325	-	0.49	1.46	0.032	5.9	0.001
326	-	0.40	1.10	0.018	11.9	0.002
339	-	0.64	1.36	0.031	-7.1	0.001
339	10	0.43	1.18	0.018	5.2	0.001
339	20	0.45	1.20	0.016	8.4	0.002
340	-	0.42	1.01	0.030	10.6	0.004
340	-	0.44	1.18	0.012	4.1	0.002
340	30	0.56	1.52	0.023	-2.0	0.001
341	10	0.63	1.45	0.047	-7.2	0.002
342	-	0.42	1.28	0.035	11.0	0.003
359	-	0.43	0.91	0.017	4.3	0.001
360	-	0.46	1.08	0.022	3.8	0.002
361	-	0.39	0.68	0.031	5.6	0.002

## A.2 Emissions Experiments Engine Data

Table A.4: Experimental data from emissions experiments.

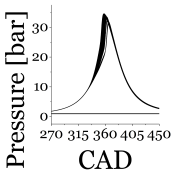
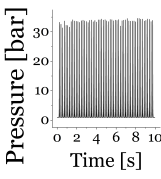
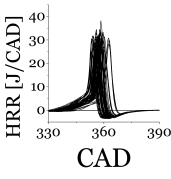
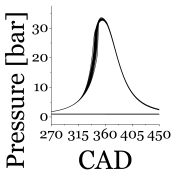
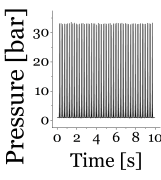
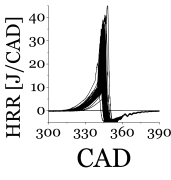
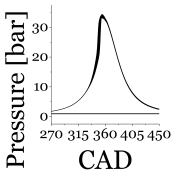
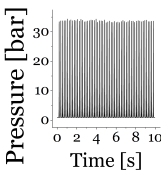
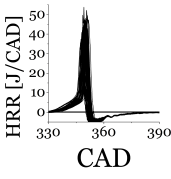
<p>Expt. 1  <math>T_{in} = 262^{\circ}\text{C}</math>            SA <math>50^{\circ}</math> BTDC  <math>\phi = 0.56</math></p>	 <p>Pressure [bar] CAD</p>	 <p>Pressure [bar] Time [s]</p>	 <p>HRR [J/CAD] CAD</p>
<p>Expt. 2  <math>T_{in} = 274^{\circ}\text{C}</math>            SA <math>70^{\circ}</math> BTDC  <math>\phi = 0.59</math></p>	 <p>Pressure [bar] CAD</p>	 <p>Pressure [bar] Time [s]</p>	 <p>HRR [J/CAD] CAD</p>
<p>Expt. 3  <math>T_{in} = 274^{\circ}\text{C}</math>            SA <math>50^{\circ}</math> BTDC  <math>\phi = 0.59</math></p>	 <p>Pressure [bar] CAD</p>	 <p>Pressure [bar] Time [s]</p>	 <p>HRR [J/CAD] CAD</p>

Table A.4: Experimental data from emissions experiments.

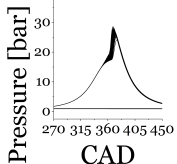
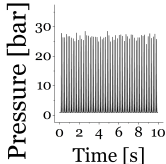
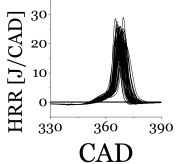
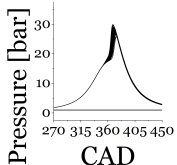
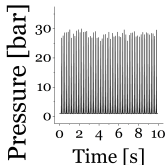
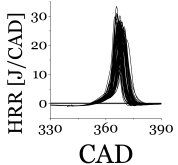
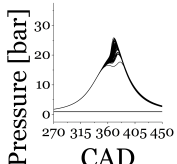
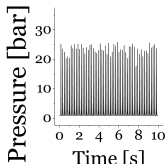
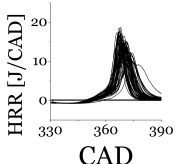
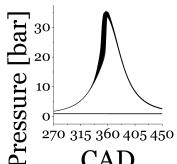
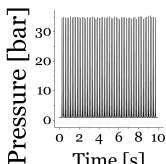
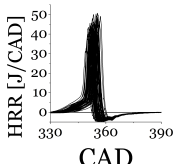
<p>Expt. 4  <math>T_{in} = 275^{\circ}\text{C}</math>  SA <math>20^{\circ}</math> BTDC  <math>\phi = 0.55</math></p>	 <p>Pressure [bar] CAD</p>	 <p>Pressure [bar] Time [s]</p>	 <p>HRR [J/CAD] CAD</p>
<p>Expt. 5  <math>T_{in} = 280^{\circ}\text{C}</math>  SA <math>20^{\circ}</math> BTDC  <math>\phi = 0.57</math></p>	 <p>Pressure [bar] CAD</p>	 <p>Pressure [bar] Time [s]</p>	 <p>HRR [J/CAD] CAD</p>
<p>Expt. 6  <math>T_{in} = 281^{\circ}\text{C}</math>  SA <math>30^{\circ}</math> BTDC  <math>\phi = 0.52</math></p>	 <p>Pressure [bar] CAD</p>	 <p>Pressure [bar] Time [s]</p>	 <p>HRR [J/CAD] CAD</p>
<p>Expt. 7  <math>T_{in} = 283^{\circ}\text{C}</math>  SA <math>50^{\circ}</math> BTDC  <math>\phi = 0.59</math></p>	 <p>Pressure [bar] CAD</p>	 <p>Pressure [bar] Time [s]</p>	 <p>HRR [J/CAD] CAD</p>

Table A.4: Experimental data from emissions experiments.

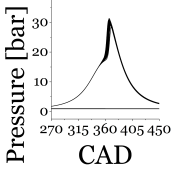
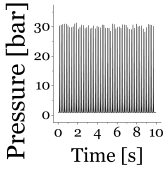
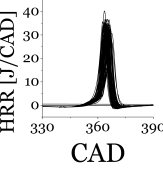
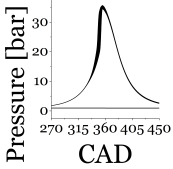
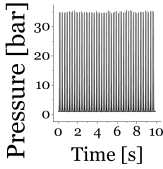
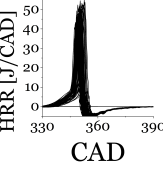
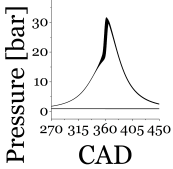
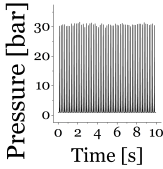
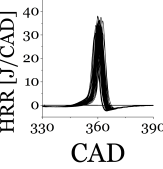
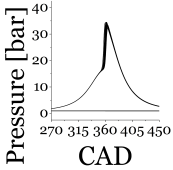
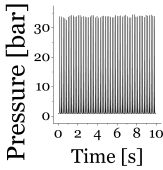
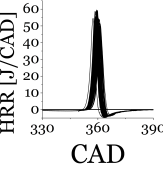
<p>Expt. 8  <math>T_{in} = 297^{\circ}\text{C}</math>            SA <math>20^{\circ}</math> BTDC  <math>\phi = 0.60</math></p>	 <p>Pressure [bar] CAD</p>	 <p>Pressure [bar] Time [s]</p>	 <p>HRR [J/CAD] CAD</p>
<p>Expt. 9  <math>T_{in} = 297^{\circ}\text{C}</math>            SA <math>50^{\circ}</math> BTDC  <math>\phi = 0.59</math></p>	 <p>Pressure [bar] CAD</p>	 <p>Pressure [bar] Time [s]</p>	 <p>HRR [J/CAD] CAD</p>
<p>Expt. 10  <math>T_{in} = 303^{\circ}\text{C}</math>            SA <math>30^{\circ}</math> BTDC  <math>\phi = 0.54</math></p>	 <p>Pressure [bar] CAD</p>	 <p>Pressure [bar] Time [s]</p>	 <p>HRR [J/CAD] CAD</p>
<p>Expt. 11  <math>T_{in} = 304^{\circ}\text{C}</math>            SA <math>10^{\circ}</math> BTDC  <math>\phi = 0.60</math></p>	 <p>Pressure [bar] CAD</p>	 <p>Pressure [bar] Time [s]</p>	 <p>HRR [J/CAD] CAD</p>

Table A.4: Experimental data from emissions experiments.

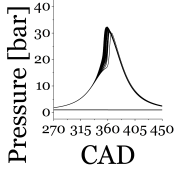
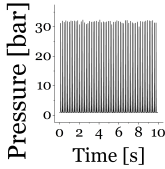
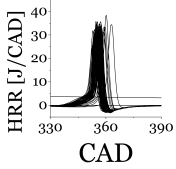
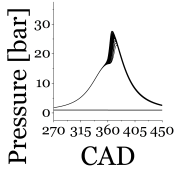
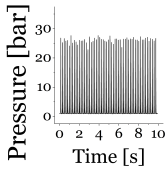
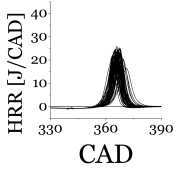
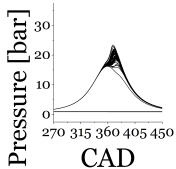
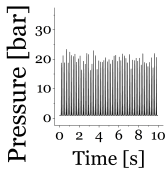
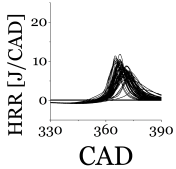
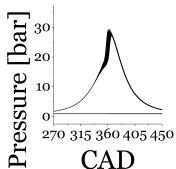
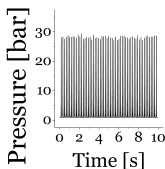
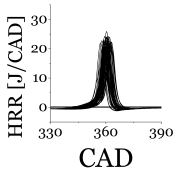
<p>Expt. 12  <math>T_{in} = 319^{\circ}\text{C}</math>  SA <math>50^{\circ}</math> BTDC  <math>\phi = 0.52</math></p>	 <p>Pressure [bar] CAD</p>	 <p>Pressure [bar] Time [s]</p>	 <p>HRR [J/CAD] CAD</p>
<p>Expt. 13  <math>T_{in} = 320^{\circ}\text{C}</math>  SA <math>20^{\circ}</math> BTDC  <math>\phi = 0.51</math></p>	 <p>Pressure [bar] CAD</p>	 <p>Pressure [bar] Time [s]</p>	 <p>HRR [J/CAD] CAD</p>
<p>Expt. 14  <math>T_{in} = 320^{\circ}\text{C}</math>  SA <math>50^{\circ}</math> BTDC  <math>\phi = 0.42</math></p>	 <p>Pressure [bar] CAD</p>	 <p>Pressure [bar] Time [s]</p>	 <p>HRR [J/CAD] CAD</p>
<p>Expt. 15  <math>T_{in} = 320^{\circ}\text{C}</math>  SA <math>50^{\circ}</math> BTDC  <math>\phi = 0.48</math></p>	 <p>Pressure [bar] CAD</p>	 <p>Pressure [bar] Time [s]</p>	 <p>HRR [J/CAD] CAD</p>

Table A.4: Experimental data from emissions experiments.

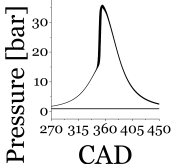
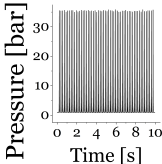
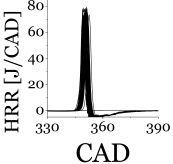
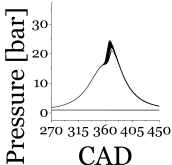
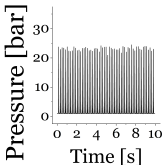
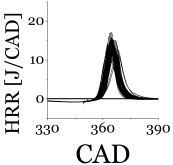
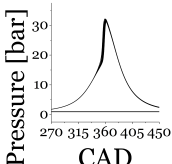
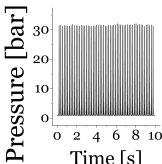
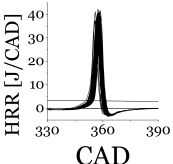
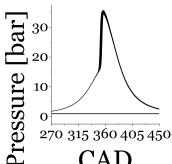
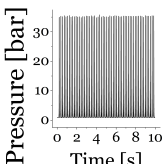
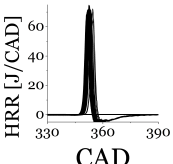
<p>Expt. 16  <math>T_{in} = 321^{\circ}\text{C}</math>            Unassisted  <math>\phi = 0.63</math></p>	 <p>Pressure [bar] CAD</p>	 <p>Pressure [bar] Time [s]</p>	 <p>HRR [J/CAD] CAD</p>
<p>Expt. 17  <math>T_{in} = 321^{\circ}\text{C}</math>            SA <math>10^{\circ}</math> BTDC  <math>\phi = 0.44</math></p>	 <p>Pressure [bar] CAD</p>	 <p>Pressure [bar] Time [s]</p>	 <p>HRR [J/CAD] CAD</p>
<p>Expt. 18  <math>T_{in} = 321^{\circ}\text{C}</math>            SA <math>30^{\circ}</math> BTDC  <math>\phi = 0.55</math></p>	 <p>Pressure [bar] CAD</p>	 <p>Pressure [bar] Time [s]</p>	 <p>HRR [J/CAD] CAD</p>
<p>Expt. 19  <math>T_{in} = 324^{\circ}\text{C}</math>            SA <math>10^{\circ}</math> BTDC  <math>\phi = 0.63</math></p>	 <p>Pressure [bar] CAD</p>	 <p>Pressure [bar] Time [s]</p>	 <p>HRR [J/CAD] CAD</p>

Table A.4: Experimental data from emissions experiments.

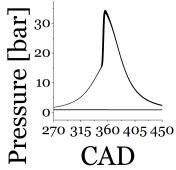
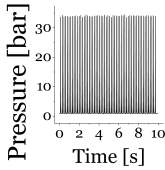
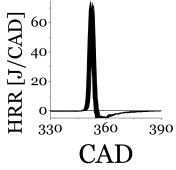
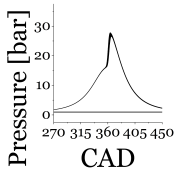
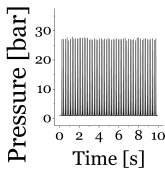
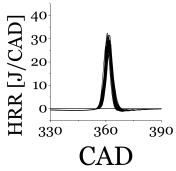
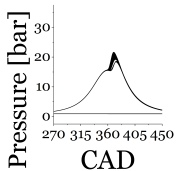
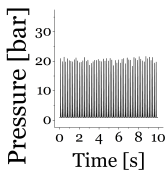
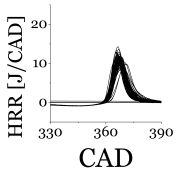
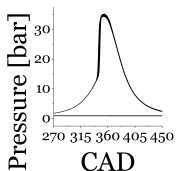
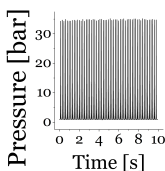
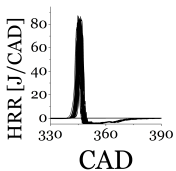
<p>Expt. 20  <math>T_{in} = 325^{\circ}\text{C}</math>                      Unassisted  <math>\phi = 0.61</math></p>	 <p>Pressure [bar] CAD</p>	 <p>Pressure [bar] Time [s]</p>	 <p>HRR [J/CAD] CAD</p>
<p>Expt. 21  <math>T_{in} = 325^{\circ}\text{C}</math>                      Unassisted  <math>\phi = 0.49</math></p>	 <p>Pressure [bar] CAD</p>	 <p>Pressure [bar] Time [s]</p>	 <p>HRR [J/CAD] CAD</p>
<p>Expt. 22  <math>T_{in} = 326^{\circ}\text{C}</math>                      Unassisted  <math>\phi = 0.40</math></p>	 <p>Pressure [bar] CAD</p>	 <p>Pressure [bar] Time [s]</p>	 <p>HRR [J/CAD] CAD</p>
<p>Expt. 23  <math>T_{in} = 339^{\circ}\text{C}</math>                      Unassisted  <math>\phi = 0.64</math></p>	 <p>Pressure [bar] CAD</p>	 <p>Pressure [bar] Time [s]</p>	 <p>HRR [J/CAD] CAD</p>

Table A.4: Experimental data from emissions experiments.

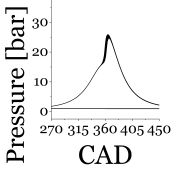
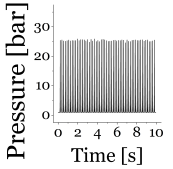
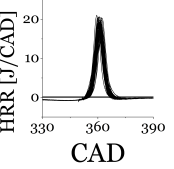
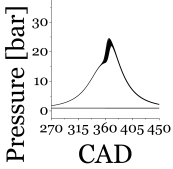
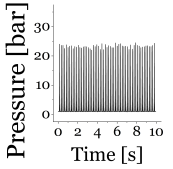
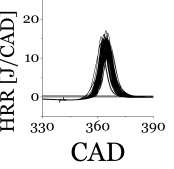
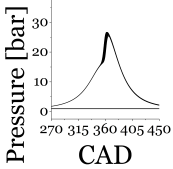
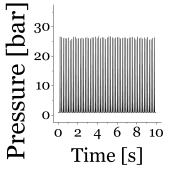
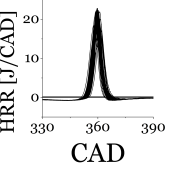
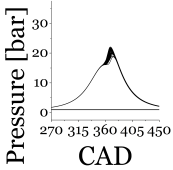
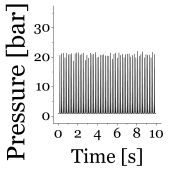
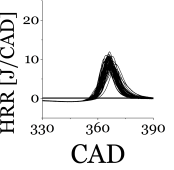
<p>Expt. 24  <math>T_{in} = 339^{\circ}\text{C}</math>            SA <math>10^{\circ}</math> BTDC  <math>\phi = 0.43</math></p>	 <p>Pressure [bar] CAD</p>	 <p>Pressure [bar] Time [s]</p>	 <p>HRR [J/CAD] CAD</p>
<p>Expt. 25  <math>T_{in} = 339^{\circ}\text{C}</math>            SA <math>20^{\circ}</math> BTDC  <math>\phi = 0.45</math></p>	 <p>Pressure [bar] CAD</p>	 <p>Pressure [bar] Time [s]</p>	 <p>HRR [J/CAD] CAD</p>
<p>Expt. 26  <math>T_{in} = 340^{\circ}\text{C}</math>            Unassisted  <math>\phi = 0.42</math></p>	 <p>Pressure [bar] CAD</p>	 <p>Pressure [bar] Time [s]</p>	 <p>HRR [J/CAD] CAD</p>
<p>Expt. 27  <math>T_{in} = 340^{\circ}\text{C}</math>            Unassisted  <math>\phi = 0.44</math></p>	 <p>Pressure [bar] CAD</p>	 <p>Pressure [bar] Time [s]</p>	 <p>HRR [J/CAD] CAD</p>



Table A.4: Experimental data from emissions experiments.

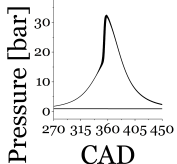
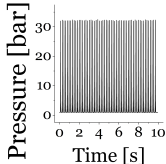
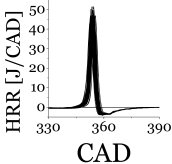
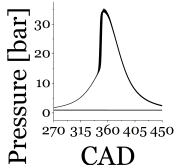
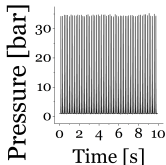
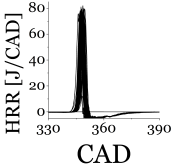
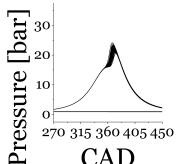
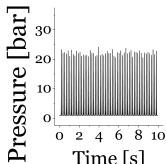
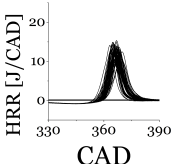
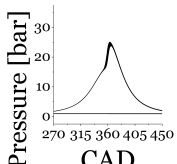
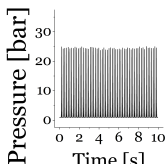
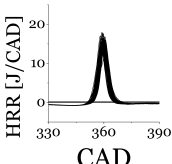
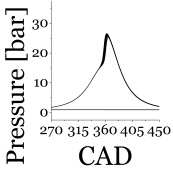
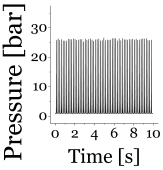
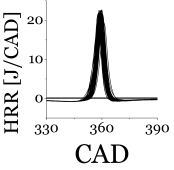
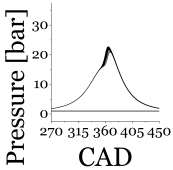
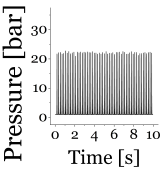
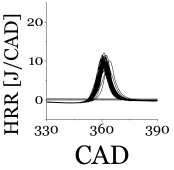
<p>Expt. 28  <math>T_{in} = 340^{\circ}\text{C}</math>                      SA <math>30^{\circ}</math> BTDC  <math>\phi = 0.56</math></p>	 <p>Pressure [bar] CAD</p>	 <p>Pressure [bar] Time [s]</p>	 <p>HRR [J/CAD] CAD</p>
<p>Expt. 29  <math>T_{in} = 341^{\circ}\text{C}</math>                      SA <math>10^{\circ}</math> BTDC  <math>\phi = 0.63</math></p>	 <p>Pressure [bar] CAD</p>	 <p>Pressure [bar] Time [s]</p>	 <p>HRR [J/CAD] CAD</p>
<p>Expt. 30  <math>T_{in} = 342^{\circ}\text{C}</math>                      Unassisted  <math>\phi = 0.42</math></p>	 <p>Pressure [bar] CAD</p>	 <p>Pressure [bar] Time [s]</p>	 <p>HRR [J/CAD] CAD</p>
<p>Expt. 31  <math>T_{in} = 359^{\circ}\text{C}</math>                      Unassisted  <math>\phi = 0.43</math></p>	 <p>Pressure [bar] CAD</p>	 <p>Pressure [bar] Time [s]</p>	 <p>HRR [J/CAD] CAD</p>

Table A.4: Experimental data from emissions experiments.

<p>Expt. 32  <math>T_{in} = 360^{\circ}\text{C}</math>            Unassisted  <math>\phi = 0.46</math></p>	 <p>Pressure [bar] CAD</p>	 <p>Pressure [bar] Time [s]</p>	 <p>HRR [J/CAD] CAD</p>
<p>Expt. 33  <math>T_{in} = 361^{\circ}\text{C}</math>            SA <math>50^{\circ}</math> BTDC  <math>\phi = 0.39</math></p>	 <p>Pressure [bar] CAD</p>	 <p>Pressure [bar] Time [s]</p>	 <p>HRR [J/CAD] CAD</p>

### A.3 Imaging Experiments Engine Data

Table A.5: Experimental data from imaging experiments.

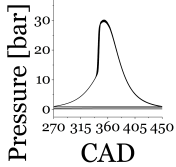
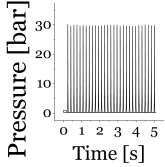
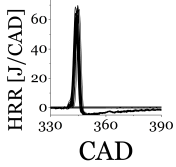
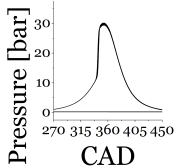
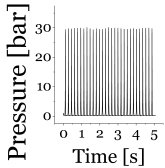
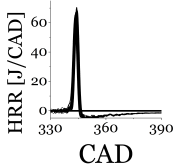
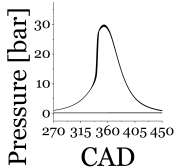
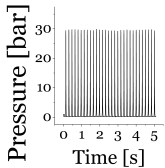
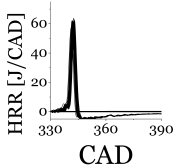
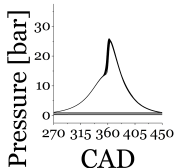
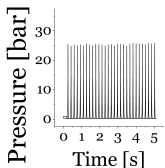
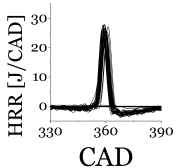
<p>Expt. R0  <math>T_{in} = 320^{\circ}\text{C}</math>            Unassisted  <math>\phi = 0.58</math></p>	 <p>Pressure [bar] CAD</p>	 <p>Pressure [bar] Time [s]</p>	 <p>HRR [J/CAD] CAD</p>
<p>Expt. R20  <math>T_{in} = 320^{\circ}\text{C}</math>            SA <math>20^{\circ}</math> BTDC  <math>\phi = 0.59</math></p>	 <p>Pressure [bar] CAD</p>	 <p>Pressure [bar] Time [s]</p>	 <p>HRR [J/CAD] CAD</p>
<p>Expt. R40  <math>T_{in} = 320^{\circ}\text{C}</math>            SA <math>40^{\circ}</math> BTDC  <math>\phi = 0.58</math></p>	 <p>Pressure [bar] CAD</p>	 <p>Pressure [bar] Time [s]</p>	 <p>HRR [J/CAD] CAD</p>
<p>Expt. M0  <math>T_{in} = 320^{\circ}\text{C}</math>            Unassisted  <math>\phi = 0.52</math></p>	 <p>Pressure [bar] CAD</p>	 <p>Pressure [bar] Time [s]</p>	 <p>HRR [J/CAD] CAD</p>

Table A.5: Experimental data from imaging experiments.

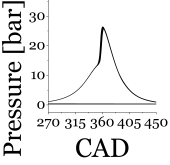
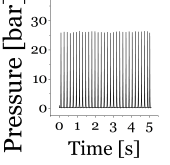
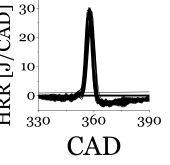
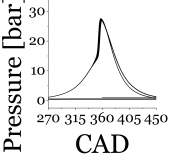
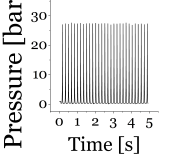
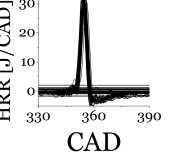
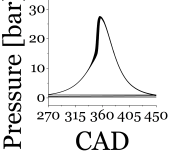
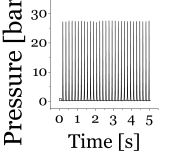
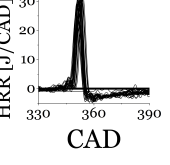
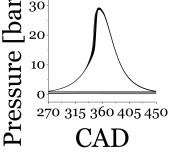
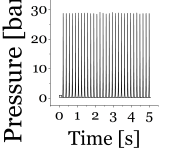
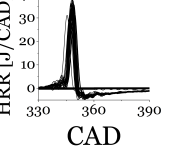
<p>Expt. M20  <math>T_{in} = 320^{\circ}\text{C}</math>            SA <math>20^{\circ}</math> BTDC  <math>\phi = 0.51</math></p>	 <p>Pressure [bar] CAD</p>	 <p>Pressure [bar] Time [s]</p>	 <p>HRR [J/CAD] CAD</p>
<p>Expt. M30  <math>T_{in} = 320^{\circ}\text{C}</math>            SA <math>30^{\circ}</math> BTDC  <math>\phi = 0.53</math></p>	 <p>Pressure [bar] CAD</p>	 <p>Pressure [bar] Time [s]</p>	 <p>HRR [J/CAD] CAD</p>
<p>Expt. M40  <math>T_{in} = 320^{\circ}\text{C}</math>            SA <math>40^{\circ}</math> BTDC  <math>\phi = 0.51</math></p>	 <p>Pressure [bar] CAD</p>	 <p>Pressure [bar] Time [s]</p>	 <p>HRR [J/CAD] CAD</p>
<p>Expt. M50  <math>T_{in} = 320^{\circ}\text{C}</math>            SA <math>50^{\circ}</math> BTDC  <math>\phi = 0.53</math></p>	 <p>Pressure [bar] CAD</p>	 <p>Pressure [bar] Time [s]</p>	 <p>HRR [J/CAD] CAD</p>

Table A.5: Experimental data from imaging experiments.

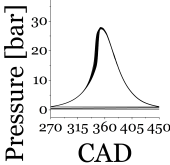
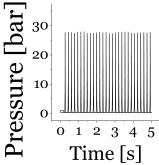
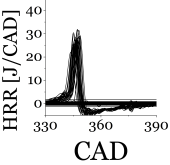
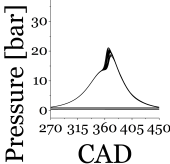
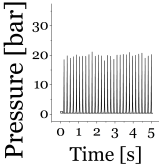
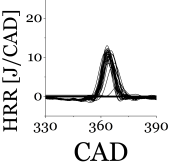
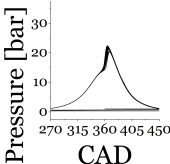
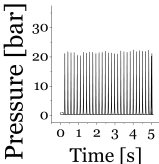
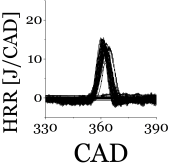
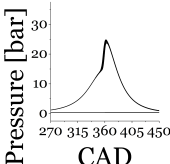
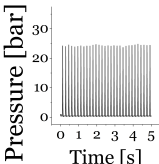
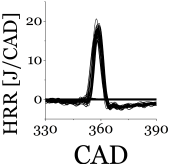
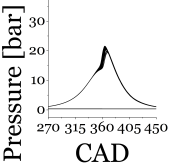
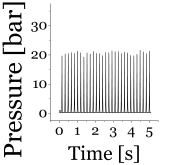
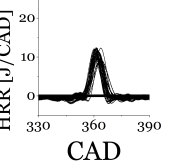
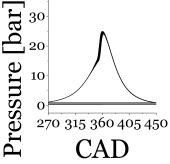
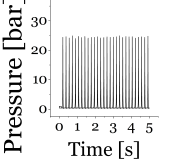
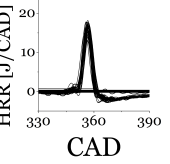
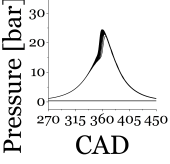
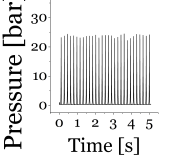
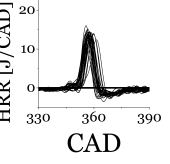
<p>Expt. M60  <math>T_{in} = 320^{\circ}\text{C}</math>  SA 60° BTDC  <math>\phi = 0.53</math></p>	 <p>Pressure [bar] CAD</p>	 <p>Pressure [bar] Time [s]</p>	 <p>HRR [J/CAD] CAD</p>
<p>Expt. L0  <math>T_{in} = 320^{\circ}\text{C}</math>  Unassisted  <math>\phi = 0.46</math></p>	 <p>Pressure [bar] CAD</p>	 <p>Pressure [bar] Time [s]</p>	 <p>HRR [J/CAD] CAD</p>
<p>Expt. L20  <math>T_{in} = 320^{\circ}\text{C}</math>  SA 20° BTDC  <math>\phi = 0.45</math></p>	 <p>Pressure [bar] CAD</p>	 <p>Pressure [bar] Time [s]</p>	 <p>HRR [J/CAD] CAD</p>
<p>Expt. L30  <math>T_{in} = 320^{\circ}\text{C}</math>  SA 30° BTDC  <math>\phi = 0.45</math></p>	 <p>Pressure [bar] CAD</p>	 <p>Pressure [bar] Time [s]</p>	 <p>HRR [J/CAD] CAD</p>

Table A.5: Experimental data from imaging experiments.

<p>Expt. L40  <math>T_{in} = 320^{\circ}\text{C}</math>  SA <math>40^{\circ}</math> BTDC  <math>\phi = 0.45</math></p>	 <p>Pressure [bar] CAD</p>	 <p>Pressure [bar] Time [s]</p>	 <p>HRR [J/CAD] CAD</p>
<p>Expt. L50  <math>T_{in} = 320^{\circ}\text{C}</math>  SA <math>50^{\circ}</math> BTDC  <math>\phi = 0.45</math></p>	 <p>Pressure [bar] CAD</p>	 <p>Pressure [bar] Time [s]</p>	 <p>HRR [J/CAD] CAD</p>
<p>Expt. L60  <math>T_{in} = 320^{\circ}\text{C}</math>  SA <math>60^{\circ}</math> BTDC  <math>\phi = 0.45</math></p>	 <p>Pressure [bar] CAD</p>	 <p>Pressure [bar] Time [s]</p>	 <p>HRR [J/CAD] CAD</p>

# Bibliography

- [1] K. Epping, S. Aceves, R. Bechtold, and J. Dec. The potential of hcci combustion for high efficiency and low emissions. *SAE*, 2002-01-1923, 2002.
- [2] M. Christensen, P. Einewall, and B. Johansson. Homogeneous charge compression ignition (hcci) using iso-octane, ethanol and natural gas - a comparison to spark ignition operation. *SAE*, 972874, 1997. PT: J.
- [3] H. Santoso, J. Matthews, and W. Cheng. Managing si/hcci dual-mode engine operation. *SAE*, 2005-01-0162, April 2005. PT: J.
- [4] M. Weinrotter, E. Winter, K. Iskra, T. Neger, J. Olofsson, H. Seyfried, M. Alden, M. Lackner, F. Winter, A. Vressner, A. Hultqvist, and B. Johansson. Optical diagnostics of laser-induced and spark plug-assisted hcci combustion. *SAE*, 2005-01-0129, April 2005. PT: J.
- [5] J. Hyvonen, G. Haraldsson, and B. Johansson. Operating conditions using spark assisted hcci combustion during

- combustion mode transfer to si in a multi-cylinder vcr-hcci engine. *SAE*, 2005-01-0109, April 2005. PT: J.
- [6] A. Berntsson and I. Denbratt. Spark assisted hcci combustion using a stratified hydrogen charge. *SAE*, 2005-24-039, September 2005. PT: J.
- [7] Z. Wang, J. X Wang, S. J Shuai, and Q. J Ma. Effects of spark ignition and stratified charge on gasoline hcci combustion with direct injection. *SAE*, 2005-01-0137, April 2005. PT: J.
- [8] R. Wagner, K. Edwards, C. Daw, J. Green, and B. Bunting. On the nature of cyclic dispersion in spark assisted hcci combustion. *SAE*, 2006-01-0418, April 2006. PT: J.
- [9] Vinod Kumar Natarajan. Spark-assisted compression ignition: an experimental investigation into how spark ignition advances combustion phasing in gasoline hcci engines, 2006.
- [10] Bradley T. Zigler. *An experimental investigation of the ignition properties of low temperature combustion in an optical engine*. PhD thesis, University of Michigan - Ann Arbor, Department of Mechanical Engineering, 2008.
- [11] F. Agrell, H. E Angstrom, B. Eriksson, J. Wikander, and J. Linderyd. Transient control of hcci-combustion by aid of variable valve timing through the use of an engine state corrected ca50-controller combined with an in-cylinder state estimator estimating lambda. *SAE*, 2005-01-2128, 2005.
- [12] G. Haraldsson, J. Hyvonen, P. Tunestal, and B. Johansson. Hcci combustion phasing with closed-loop combustion



- control using variable compression ratio in a multi-cylinder engine. *SAE*, 2003-01-1830, 2003. PT: J.
- [13] M. Christensen, J. Hultqvist, and B. Johansson. Demonstrating the multi-fuel capability of a homogeneous charge compression ignition engine with variable compression ratio. *SAE*, 1999-01-3679, 1999. PT: J.
- [14] M. Milovanovic, D. Blundell, S. Gedge, and J. Turner. Si-hcci-si mode transition at different engine operating conditions. *SAE*, 2005-01-0156, April 2005. PT: J.
- [15] Andreas W. Berntsson, Mats Andersson, Daniel Dahl, and Ingemar Denbratt. A lif-study of oh in the negative valve overlap of a spark-assisted hcci combustion engine. *SAE*, 2008-01-0037, 2008.
- [16] H. Persson, A. Hultqvist, B. Johansson, and A. Remon. Investigation of the early flame development in spark assisted hcci combustion using high speed chemiluminescence imag. *SAE*, 2007-01-0212, 2007.
- [17] P. G. Aleiferis, A. G. Charlambides, Y. Hardalupas, A. M. K. P. Taylor, and Urata Y. Autoignition initiation and development of n-heptane hcci combustion assisted by inlet air heating, internal egr or spark discharge: An optical investigation. *SAE*, 2007-01-3273, 2007.
- [18] B. T. Zigler, S. M. Walton, D. Assanis, E. Perez, and M. S. Wooldridge. Crank-angle resolved imaging of hcci phenomena in a single-cylinder research engine. The Combustion Institute 31st International Symposium on Combustion - Poster Session, 2006.

- [19] B. T. Zigler, S. M. Walton, D. Assanis, E. Perez, M. S. Wooldridge, and S. T. Wooldridge. An imaging study of compression ignition phenomena of iso-octane, indolene, and gasoline fuels in a single-cylinder research engine. *ASME Journal of Engineering for Gas Turbines and Power*, 130, 2008.
- [20] B. T. Zigler, S. M. Walton, X. He, J. T. Wiswall, M. S. Wooldridge, and S. T. Wooldridge. Crank-angle resolved imaging of homogeneous charge compression ignition phenomena in a single-cylinder research engine. *Proceedings of the 2006 Technical Meeting of the Central States Section of The Combustion Institute*, 2006.
- [21] Bradley T. Zigler, Stephen M. Walton, Darshan M. Karwat, Dimitris Assanis, Margaret S. Wooldridge, and Steven T. Wooldridge. A multi-axis imaging study of spark-assisted homogeneous charge compression ignition phenomena in a single-cylinder research engine. *PROCEEDINGS OF THE 2007 FALL TECHNICAL CONFERENCE OF THE ASME INTERNAL COMBUSTION ENGINE DIVISION*, page 395, 2008.
- [22] D. Sunnaborg. Design specifications summary for the sandia national laboratories optical engine. *Sandia National Laboratories*, May 1997. PT: J.
- [23] S. M. Walton, X. He, M. T. Donovan, B. T. Zigler, T. R. Palmer, M. S. Wooldridge, and A. Atreya. High-speed digital imaging of iso-octane mixtures at homogeneous charge compression ignition operating conditions. In *The Central*

- States Meeting of The Combustion Institute*, March 21-23 2004.
- [24] J. Heywood. *Internal Combustion Engine Fundamentals*. McGraw-Hill, 1988.
- [25] Peter E. Keros, Dimitris Assanis, Jill Schlechtweg, and Maragaret S. Wooldridge. Fast methods to analyze high-speed images of hcci and spark-assisted hcci ignition events. In *Proceedings of the ASME Internal Combustion Engine Division 2010 Fall Technical Conference*, 2010.
- [26] P. E. Keros, B. T. Zigler, J. T. Wiswall, S. M. Walton, and M. S. Wooldridge. An experimental investigation of the exhaust emissions from spark-assisted homogeneous charge compression ignition in a single-cylinder research engine. In *Proceedings of the ASME Internal Combustion Engine Division 2009 Spring Technical Conference*, 2009.
- [27] Katrine B. Helleburg. Spark assisted homogeneous compression combustion ignition image analysis. AUTO 503, Fall 2010.
- [28] B. T. Zigler, P. E. Keros, Dim. Assanis, and M. S. Wooldridge. An experimental investigation of the sensitivity of the ignition and combustion properties of a single-cylinder research engine to spark-assisted hcci. *International Journal of Engine Research*, 2011 (in press).